ARL-TR-9813 ● Oct 2023

Rate-Dependent Shear Response during Off-Axis Loading of Fiber and Film-Based UHMWPE Composites

by C Allan Gunnarsson, Stephen L Alexander, and Tusit Weerasooriya

DISTRIBUTION STATEMENT A. Approved for public release: distribution unlimited.

NOTICES

Disclaimers

The research reported in this document was performed in connection with contract/instrument W15P7T-19-D-0126 with the DEVCOM Army Research Laboratory.

The findings in this report are not to be construed as an official Department of the Army position unless so designated by other authorized documents. The views and conclusions contained in this document are those of SURVICE Engineering Company and the DEVCOM Army Research Laboratory.

Citation of manufacturer's or trade names does not constitute an official endorsement or approval of the use thereof.

Destroy this report when it is no longer needed. Do not return it to the originator.

ARL-TR-9813 ● OCT 2023

Rate-Dependent Shear Response during Off-Axis Loading of Fiber and Film-Based UHMWPE Composites

C Allan Gunnarsson and Tusit Weerasooriya
DEVCOM Army Research Laboratory

Stephen L Alexander
SURVICE Engineering Company

DISTRIBUTION STATEMENT A. Approved for public release: distribution unlimited.

REPORT DOCUMENTATION PAGE

1. REPORT DATE	2. REPORT TYPE	3. DATES COVERED	
		START DATE	END DATE
October 2023	Technical Report	1 April 2022	1 July 2023

4. TITLE AND SUBTITLE
Rate-Dependent Shear Response during Off-Axis Loading of Fiber and Film-Based UHMWPE Composites

5a. CONTRACT NUMBER	5b. GRANT NUMBER	5c. PROGRAM ELEMENT NUMBER
W15P7T-19-D-0126		
5d. PROJECT NUMBER	**5e. TASK NUMBER**	**5f. WORK UNIT NUMBER**

6. AUTHOR(S)
C Allan Gunnarsson, Stephen L Alexander, and Tusit Weerasooriya

7. PERFORMING ORGANIZATION NAME(S) AND ADDRESS(ES)	8. PERFORMING ORGANIZATION REPORT NUMBER
DEVCOM Army Research Laboratory ATTN: FCDD-RLA-TB Aberdeen Proving Ground, MD 21005	ARL-TR-9813

9. SPONSORING/MONITORING AGENCY NAME(S) AND ADDRESS(ES)	10. SPONSOR/MONITOR'S ACRONYM(S)	11. SPONSOR/MONITOR'S REPORT NUMBER(S)

12. DISTRIBUTION/AVAILABILITY STATEMENT
DISTRIBUTION STATEMENT A. Approved for public release: distribution unlimited.

13. SUPPLEMENTARY NOTES
ORCID IDs): C Allan Gunnarsson, 0000-0002-8472-5193; Tusit Weerasooriya, 0000-0003-3299-2166

14. ABSTRACT
A novel experimental method was developed to characterize the interlaminar shear response of ultra-high-molecular-weight polyethylene (UHMWPE) composites as a function of loading rate from low to high rate. Shear failure was induced by loading specimens at different off-axis angles relative to the plane of the unidirectional layers. The method was applied to two different classes of UHMWPE materials: Dyneema HB25 consisting of traditional SK76 fiber-based plies and the newer film-based Tensylon HSBD-30A. The method allowed for full-field deformation of the specimen surface to be recorded during loading, enabling the use of digital image correlation postprocessing to obtain contours of the evolution of maximum shear strain. Specimens showed increasing stiffness and strength with loading rate. Increasing the loading rate also induced a change in failure mode from ductile failure at slower rates to early localized shear failure at high rates. These experimental findings addressed a critical knowledge gap and have been used to iteratively develop rate-dependent computational models, encompassing shearing between plies and localized Mode-2 shear de-cohesion, that simulate UHMWPE rate-dependent loading.

15. SUBJECT TERMS
UHMWPE composites, high-rate compression, split Hopkinson pressure bar (SHPB), interply shear characterization, digital image correlation, DIC, off-axis material characterization, Terminal Effects

16. SECURITY CLASSIFICATION OF:			17. LIMITATION OF ABSTRACT	18. NUMBER OF PAGES
a. REPORT	b. ABSTRACT	C. THIS PAGE		
UNCLASSIFIED	UNCLASSIFIED	UNCLASSIFIED	UU	54

19a. NAME OF RESPONSIBLE PERSON	19b. PHONE NUMBER *(Include area code)*
C Allan Gunnarsson	(410) 306-1964

STANDARD FORM 298 (REV. 5/2020)
Prescribed by ANSI Std. Z39.18

Contents

List of Figures

List of Tables

Acknowledgments

The authors would like to acknowledge the contributions of the following US Army Combat Capabilities Development Command Army Research Laboratory researchers to this study: Karl Bernetich and Michael Neblett of the Composites and Hybrid Materials Branch for composite plate consolidation and specimen fabrication.

1. Introduction

Ultra-high-molecular-weight polyethylene (UHMWPE) fiber composites have been used effectively for protection. Recent studies on impact response suggest that UHMWPE films made by solid-state extrusion (SSE) may be an emerging material for use in protection (Cline and Love 2020, Reddy et al. 2020). When compared to fiber-based UHMWPE, SSE film composites cost less to manufacture and may provide equal or improved protection levels (Singletary and Lauke 2016).

Creation of computational modeling methodology that can predict the deformation and failure of composites based on UHMWPE films and fibers requires mechanistic understanding of deformation and failure response of the subscale constituent materials and mesoscale understanding of shear and tensile (mixed-mode) delamination failure. Failure initiation criteria for mixed-mode (including shear) delamination are needed to fully simulate failure of composites under high loading rates.

The shear delamination of UHMWPE has been studied previously (Meshi et al. 2016, Bogetti et al. 2017) at quasi-static loading rate. The off-axis loading experiment has been used previously to study the rate dependency of the stress–strain response for carbon fiber and S2 glass composites (Ninan et al. 2001) and carbon fabric composites (Hosur et al. 2004). The off-axis tensile behavior of carbon fiber composites has been studied (Fourest and Berthe 2021). In addition, the in-plane compressive behavior of UHMWPE has been studied as a function of loading rate, including split Hopkinson pressure bar (SHPB) experiments (Liu et al. 2019), which resulted in ply buckling and separation. However, there are no known experimental studies to obtain rate-dependent Mode-2 shear cohesive laws that govern shear delamination failure, which is a part of the mixed-mode delamination, for UHMWPE composites.

In this study, off-axis shear experiments on composites are performed to understand their interlaminar shear response (ILSR) at three different loading rates: low, intermediate, and high rate. This allows a standard compression experiment to provide shear dominant failure in the composite to address this knowledge gap. The mechanical response of both fiber- and film-based UHMWPE consolidated composite panels (Dyneema HB25 and Tensylon HSBD-30A, respectively) were studied as a function of loading rate using off-axis shear loading. The rate dependency of the composite shear behavior was quantified using traditional hydraulic test frames as well as a compressive SHPB. Imaging was used to observe the UHMWPE specimens during loading, including ultra-high-speed imaging for high-rate experiments. Digital image correlation (DIC) was used to obtain

specimen surface strain, including at high-strain rate. A separate study has utilized the loading and deformation history of several specimens in this study in simulation to allow for iteration of the shear properties until simulation results matched the experimental results (Alexander et al. 2023). The results of the current study have provided fundamental data to optimize accurate constitutive models incorporating shear in computational simulations of threat–target interactions involving UHMWPE composites.

2. Methods

2.1 Materials

Two different classes of UHMWPE materials were used in this study. In both cases, the material was supplied in the form of sheets, referred to as precursor sheets, wound into large rolls. Each precursor sheet comprised two unidirectional (UD) layers bonded together in a cross-ply (0/90) configuration. Dyneema HB25 (manufactured by DSM Protective Materials) was used as a representative of UHMWPE composite based on fiber (SK76) at the UD layer length scale. Tensylon HSBD-30A (manufactured by DuPont, and also referred to here as Tensylon 30A) was used as a representative UHMWPE composite based on a solid-state extruded film or tape at the UD layer length scale.

2.2 Specimen Fabrication

Dyneema HB25 specimens were extracted from a HB25 UHMWPE panel that had been consolidated for a previous study that had measured mechanical properties via ultrasonic characterization (Alexander and Weerasooriya 2021), where additional details regarding the HB25 panel consolidation and processing parameters can be found. Tensylon 30A specimens were extracted from a 30A panel that was consolidated following manufacturer recommendations in a confined mold; it was heated at 175 °F, 870 psi for 10 min, and at 230 °F, 2000 psi for 20 min.

Figures 1 and 2 provide schematics of a UHMWPE panel after consolidation. These figures illustrate how each panel consisted of UD layers stacked over each other in alternating 0°/90° orientations. They also define the x′-y-z′ global coordinate system. Panel and UD layer thickness refer to the dimension in the stacking direction (z′-direction in Fig. 1).

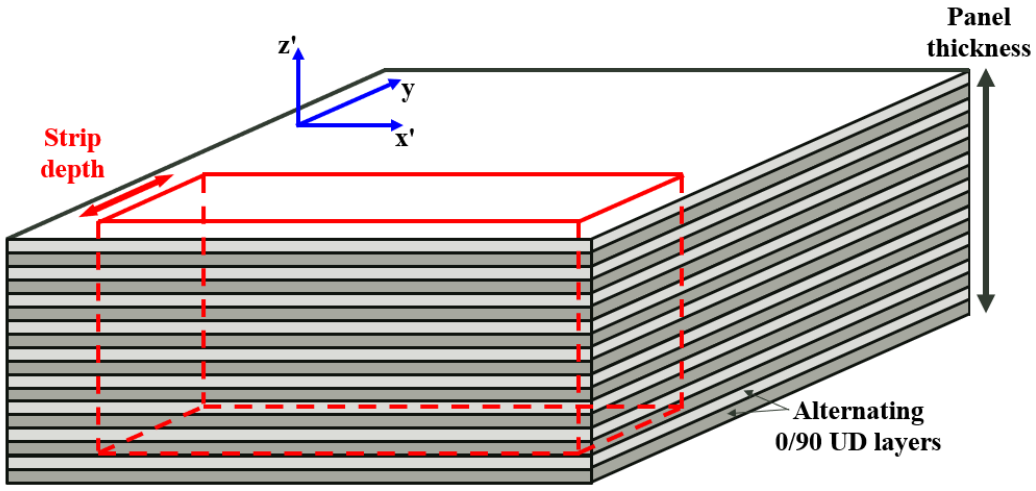

Fig. 1 Schematic of panel UD layer layup and cut orientation of panel strip. UD layer thickness is not to scale; it has been enlarged here for visualization.

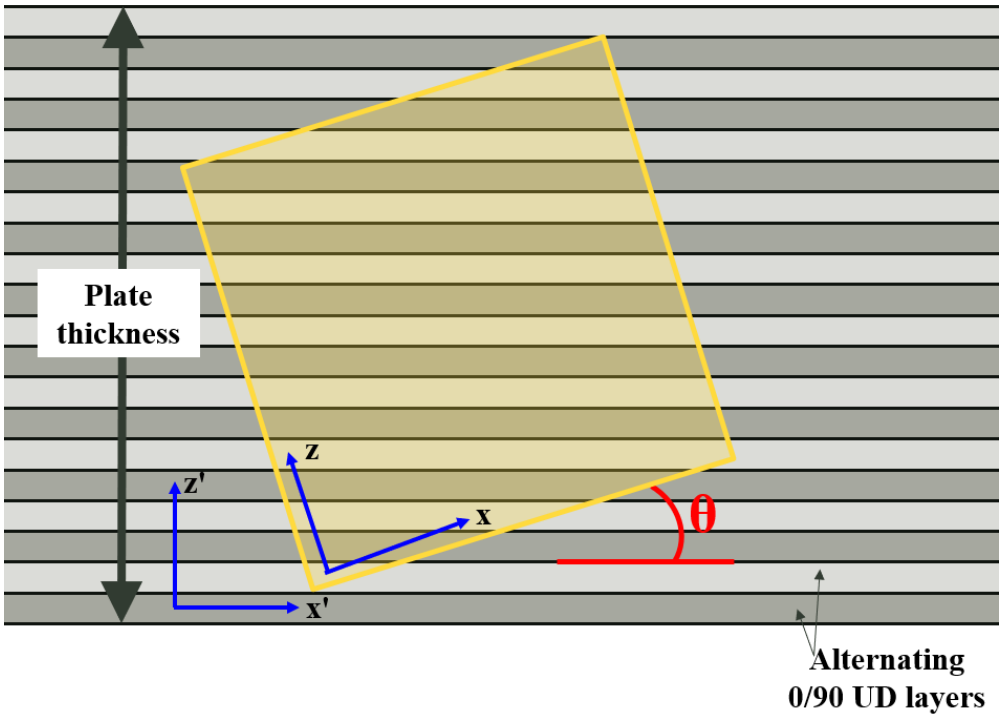

Fig. 2 Schematic of panel UD layer layup and cut orientation for off-axis shear loading specimen from strip. UD layer thickness is not to scale.

The Tensylon 30A panel was consolidated using 144 precursor sheets, corresponding to 288 UD layers. After consolidation, the 30A panel had an average thickness of 16.5 mm, with a consolidated UD layer thickness of 57.3 µm. The Dyneema HB25 panel was consolidated using 189 precursor sheets, corresponding to 378 UD layers. After consolidation, the HB25 panel had an average thickness of 25.0 mm, providing a consolidated UD layer thickness of 66.0 µm.

The consolidated composite panels were then waterjet cut into strips, with the cut axis parallel to the panel thickness axis (z′-direction in Fig. 1). For all the experiments documented here, the strip depth (y-direction in Fig. 1) was nominally 10 mm (0.4 inch).

The strips were then rotated about the x′ axis, and the off-axis shear specimens were waterjet cut out of the strip; for this cut, the cutting axis was parallel to the y-direction (defined in Fig. 1). The specimen cut is shown in yellow on Fig. 2.

The specimens were extracted at different angles relative to the plane of the UD layers. Figure 2 defines the angular orientation of the specimen as θ, such that the local coordinate system of the specimen (x-y-z) was rotated by θ relative to the global x′-y-z′ coordinate system. The off-axis shear specimens were square cut nominally 10 mm by 10 mm (0.4 by 0.4 inch) through the strip. A small tab was left to keep the specimen attached to the strip to prevent the small specimens from falling into the waterjet bath; the specimen was then separated from the strip by cutting through the tab using a band saw. Figure 3a shows the consolidated Tensylon 30A panel, after the strips had been extracted via waterjet. Figure 3b shows one of the strips cut into different off-axis orientation compression specimens (15° specimens in the example shown in the figure).

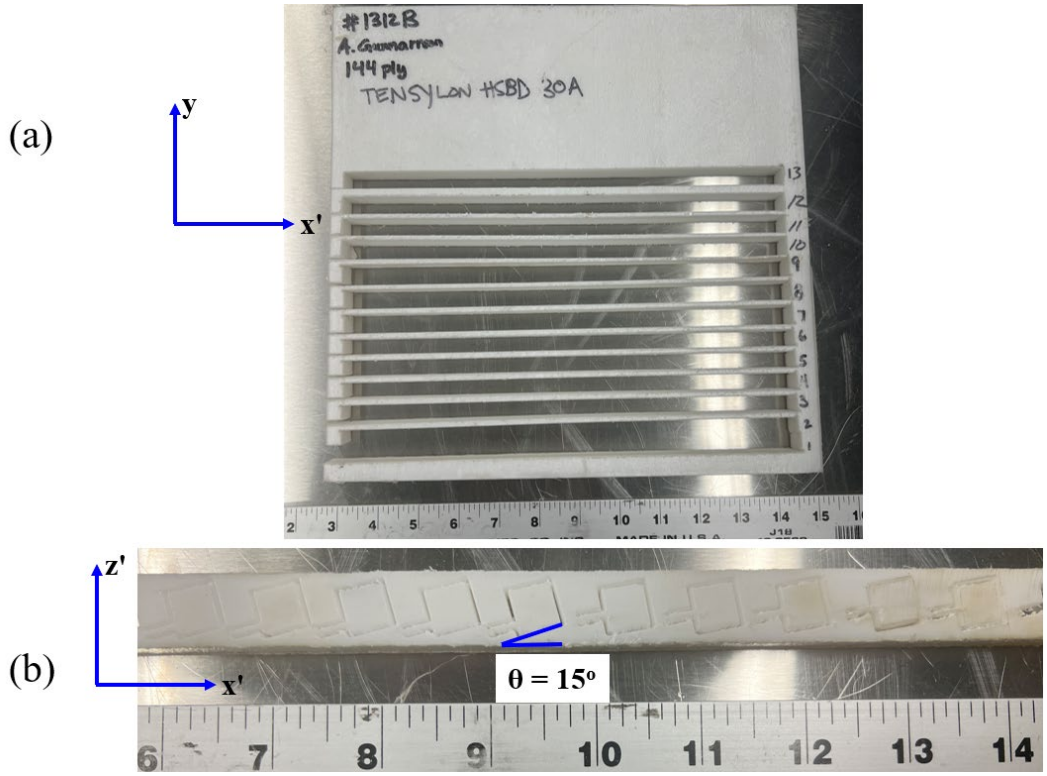

Fig. 3 (a) Consolidated composite panel after the strips had been extracted by waterjet cutting and (b) example of an extracted strip showing cubical specimens. Scale in both marked in inches.

The waterjet cutting process created rough, uneven cuts in the strip and specimen surfaces; once separated from the strip, the specimens were wet sanded using a polishing fixture to ensure the specimen surfaces were flat and parallel. After sanding, microscopy images were taken of the specimen surfaces to verify the off-axis angle (defined as θ in Fig. 2) of the specimen, as well as ensure the specimen surfaces are flat, parallel, and normal to each other (orthogonality). An image of an unsanded specimen is shown in Fig. 4. An example of a different specimen post-sanding is shown in Fig. 5. As shown in the examples, the angular orientation of the specimen was determined from the microscopy images by tracing lines along the axis of the UD layer and measuring the angle that these lines made with a line traced along the border of the specimen. The orthogonality of the specimen surfaces was evaluated by tracing the outline of the specimen (Fig. 5, left). The sanding process was iterated until orthogonality was verified and until the measured angular orientation was within 1° of the intended value.

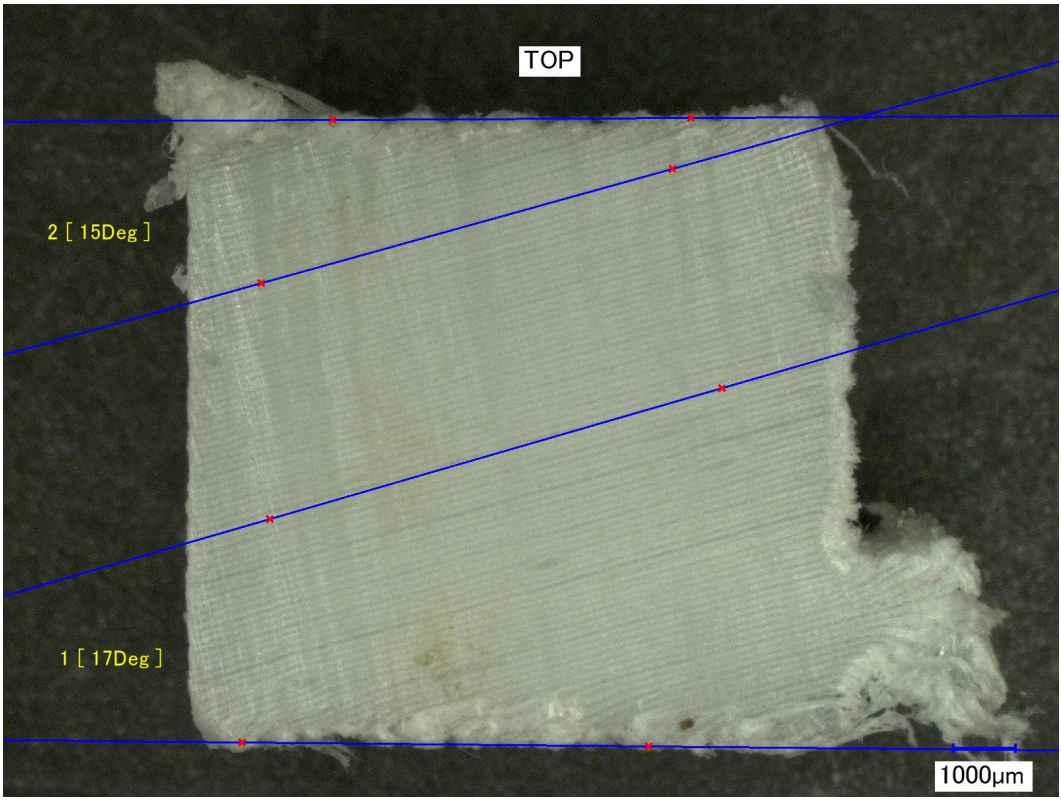

Fig. 4 Microscopy image of Tensylon 30A off-axis shear specimen at 15°, intermediate rate (TEN-15DEG-C05) as removed from panel strip without any sanding. This specimen was never sanded and was off-axis shear loaded to give a comparison to the sanded state.

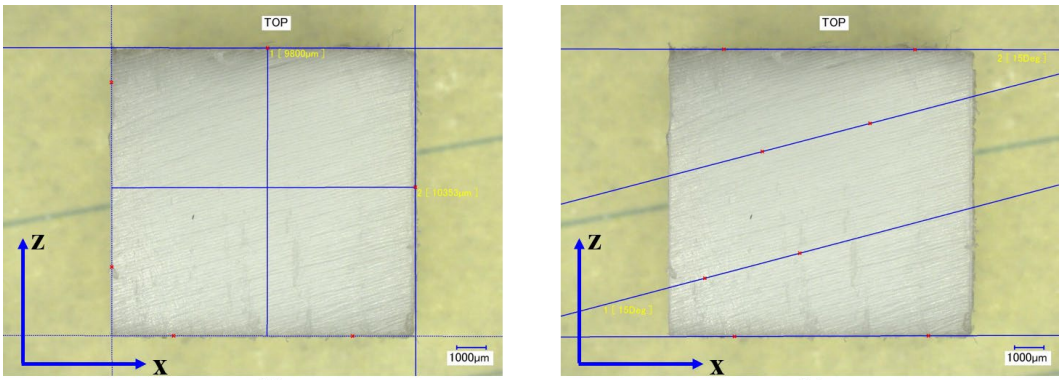

Fig. 5 Microscopy image of Tensylon 30A off-axis shear specimen at 15°, intermediate rate (TEN-15DEG-C04) after wet sanding showing (a) specimen surface orthogonality and (b) specimen ply angle

The specimen nomenclature used was MAT-ANGLE-SPECNUM, where MAT, ANGLE, and SPECNUM were specified as follows. MAT indicated the composite material type (either TEN for Tensylon 30A or HB25 for Dyneema HB25), while ANGLE corresponded to θ in Fig. 2. SPECNUM indicated the specimen number for the specific combination of MAT and ANGLE. For example, the Tensylon 30A 15° off-axis angle orientation specimens are referred to as TEN-15DEG-CXX, with the XX replaced by specimen number; for this material and angle combination, there were five specimens tested, C01–C05.

2.3 Experiments

The off-axis shear specimens were loaded in the z-direction of the specimen coordinate system (defined in Fig. 2), such that the stacking direction of the UD layer layup was at an angle to the loading axis. A schematic of the loading configuration is shown in Fig. 6, with the specimen UD layer layup off-axis angle labeled as θ. Several different off-axis angles were used: 15°, 30°, 45°, and 60°. In addition, several experiments were performed where the UD layer layup was normal to the loading axis, where θ is zero.

For all experiments, 2-D DIC was performed to quantify specimen deformation during loading. The specimens were speckled using a flat white spray-paint base coat and a black spray-paint speckle layer. Postprocessing of images was performed using commercially available software (Correlated Solutions Vic2D). For all strain analysis, the engineering strain tensor was used. The principal strains (ε_1 and ε_2) were used to calculate maximum shear strain. A series of point extractions were used to provide the maximum shear strain at the location of shear strain concentration. Figure 7 shows a maximum shear strain profile for a specimen just after peak global stress and just before the specimen failed catastrophically by shear

sliding. The ten marks (white dots) indicate the location of shear strain data extraction; these were averaged together to create an average maximum shear strain at the shear strain localization.

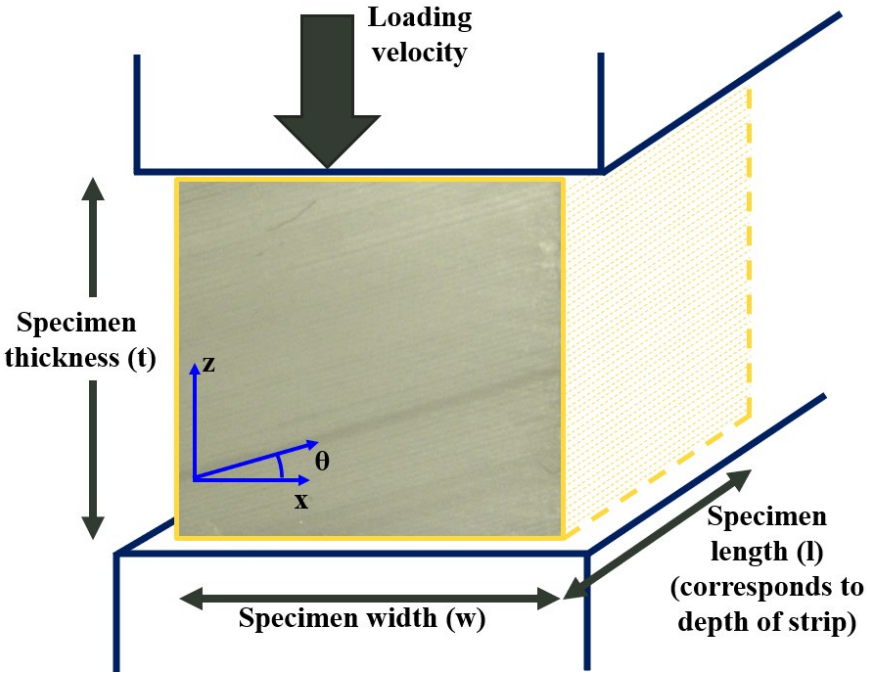

Fig. 6 Off-axis shear experiment loading and specimen orientation schematic

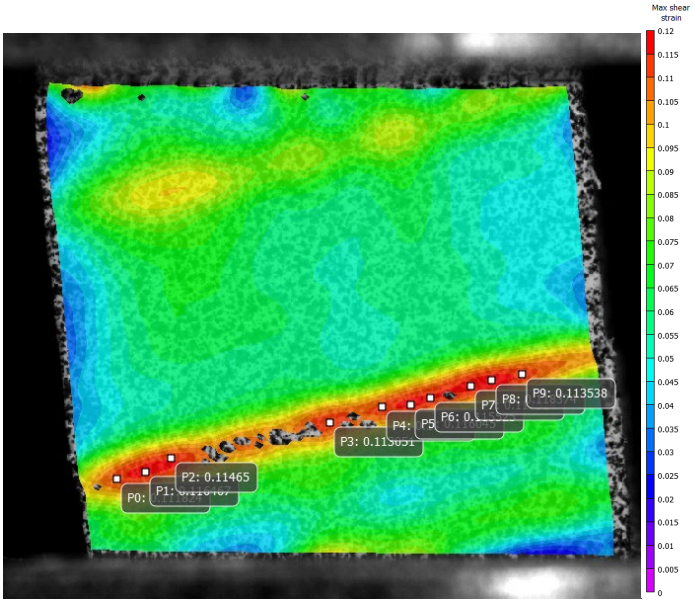

Fig. 7 Maximum shear strain profile just after peak loading and prior to sliding failure. White points indicate locations of data extraction for maximum shear strain during experiment. The data for all points are then averaged together. Color map at right ranges from 0.00 (purple) to 0.12 (red).

2.3.1 Quasi-static and Intermediate Loading Rate Experiments

For the quasi-static and intermediate strain rate experiments, a servo-hydraulic Instron test frame (Fig. 8) was used to perform compression on the off-axis shear specimens at a constant velocity; 0.005 mm/s and 5 mm/s for quasi-static and intermediate loading rates, respectively. At both quasi-static and intermediate strain rates, a framing camera captured the specimen during loading. For the quasi-static rate experiments, a FLIR 12.3-megapixel camera at 2 fps was used, and at intermediate rate, a Photron SA-5 1.0-megapixel camera at 2000 fps was used.

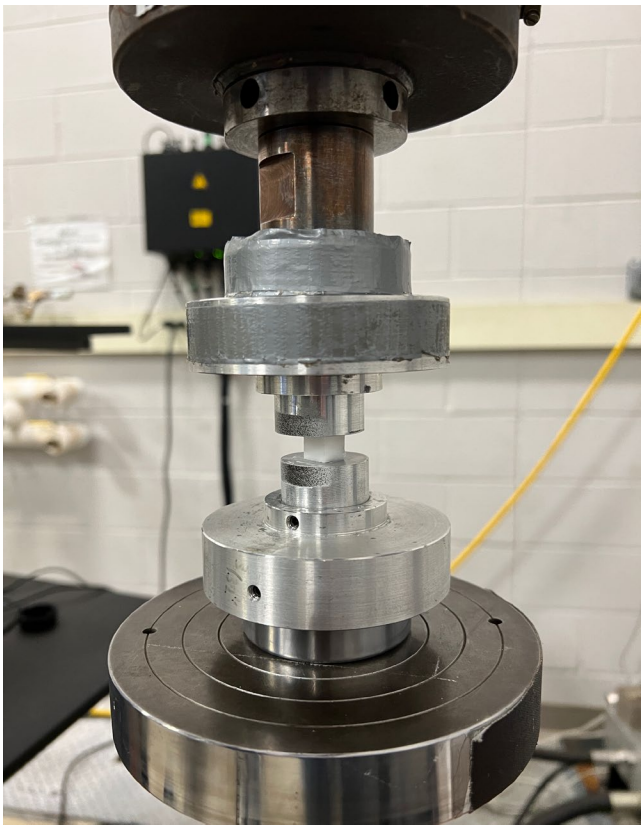

Fig. 8 Loading setup for quasi-static and intermediate rate experiments

2.3.2 High-Loading-Rate Experiments

High-loading-rate experiments were performed on the UHMWPE off-axis shear specimens using a compressive SHPB setup; details of the setup follow. The operation and theory of the SHPB are omitted for brevity, although extensive literature on this topic does exist (Schreier et al. 2009, Chen and Song 2010). Two different SHPB setups were used; the first, used for initial experiments, consisted of Maraging 350 steel 25.4-mm-diameter (1.0-inch) incident bar, transmission bar, and striker of lengths 1.83 m (72 inches), 1.83 m (72 inches), and 0.61 m (24 inches), respectively. This setup was used for four Tensylon high-rate experiments: two at normal orientation (0°) and one each at 15° and 30° off-axis angle.

The second SHPB setup, used for the remainder of high-rate experiments (Tensylon at 45° and 60°; HB25 at 0°, 15°, and 30°), consisted of Al 7075 alloy 31.8-mm-diameter (1.25-inch) incident bar, transmission bar, and striker of lengths 3.66 m (144 inches), 2.44 m (96 inches), and 0.61 m (24 inches), respectively. In addition, adapters were used at the bar end–specimen interfaces. The adapter was Al 7075, with the bar diameter on one end, and 12.7-mm square cross section at the adapter–specimen interface. The adapter was used to improve high-speed imaging of the specimen during loading by making the loading face edge almost co-planar with the specimen surface. Semiconductor gages were used on both the incident and transmission bars; semiconductor gages are known to be highly sensitive to environmental conditions, so they were calibrated with the stable resistive gages. Figure 9 shows the aluminum SHPB used for high-rate off-axis shear loading experiments, along with specimen adapters. For all high-rate experiments, wave shaping was employed to reduce dispersive effects and increase the pulse rise time to aid in achieving specimen stress equilibrium, discussed later. (For a more detailed discussion of these effects with regard to off-axis specimen configurations, the reader is directed to Ninan et al. [2001].)

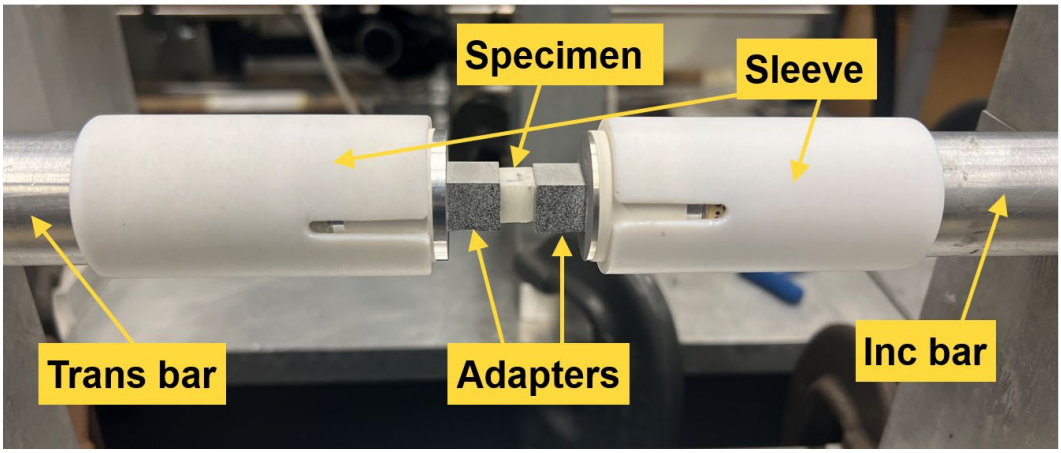

Fig. 9 SHPB setup for high-rate off-axis shear loading experiments

A Shimadzu HPV-2 ultra-high-speed camera was used at 250K fps to image the specimen during loading, allowing for postprocessing of these images to obtain specimen deformation using DIC software (Correlated Solutions VIC-2D). High-intensity LED lights were used to illuminate the specimen during loading; to avoid any heating of the specimen, these lights were turned on just prior to loading.

3. Results

The following sections document experimental data and results for the two materials, Dyneema HB25 and Tensylon 30A. Table 1 summarizes the experiments performed and results for Tensylon 30A, while Table 2 summarizes the experimental results for Dyneema HB25. The various measurements recorded in the tables are described herein.

Table 1 Summary of experimental results for Tensylon 30A off-axis shear loading experiments

Material	Off-axis angle	Velocity (mm/s)	Loading rate (kN/s)	Elastic stiffness (GPa)	Yield stress (MPa)	Normalized disp at stress peak (%)	Max shear strain (%)	Shear strain rate (/s)
Tensylon 30A	0	11966	631910	4.5	514.2	13.7	…	…
		7674.9	412640	5.2	479.1	10.0	…	…
		0.005	0.242	4.2	758.4	17.4	…	…
	15	9785.0	218540	3.0	84.0	3.6	5.6	1392.2
		0.005	0.03868	0.6	21.5	3.4	6.8	0.002
		5	53.6	1.0	78.7	8.9	11.8	0.80
		5	62.46	1.3	71.8	6.7	11.8	0.75
	30	9640.5	69934	0.7	25.8	3.7	4.9	2654
		0.005	0.01383	0.3	6.94	2.8	12.5	0.004
		5	22.96	0.5	12.5	2.9	6.1	1.395
	45	6590.8	74495	1.0	17.82	2.1	9.3	2920.8
	60	6592.5	80440	1.5	19.73	1.6	8.5	2715.2

Table 2 Summary of experimental results for Dyneema HB25 off-axis shear loading experiments

Material	Off-axis angle	Velocity (mm/s)	Loading rate (kN/s)	Elastic stiffness (GPa)	Yield stress (MPa)	Normalized disp at stress peak (%)	Max shear strain (%)	Shear strain rate (/s)
Dyneema HB25	0	3096.6	183740	3.7	308.6	8.68	…	…
	15	5530	156580	1.95	89.9	4.975	7.29	602.9
	15	0.005	0.0314	0.54	22.5	4.5	7.639	0.0012
	15	5	51.6	1.00	66.3	7.7	14.372	1.16
	30	5806.9	134830	2.34	40.1	4.08	3.75	519.1
	30	0.005	0.0091	0.19	7.7	5.76	7.33	0.00101
	30	5	16.4	0.36	17.7	7.37	9.79	1.25

At the low and intermediate rates, the displacement, velocity, and far-field global specimen load were measured using machine load cell and extension data at low and intermediate loading rates; at high rate, the bar displacement, velocities, and load were calculated using traditional SHPB strain gage data analysis. Global engineering stress was calculated by normalizing the far-field global specimen load by the cross-sectional area of the specimen measured prior to loading. Displacement was normalized using nominal specimen gage length; specimen dimensions were determined using digital calipers. Specimen shear strain was measured from DIC postprocessing of imaging acquired during loading by extracting data at a series of points at the location of shear strain concentration, as described in Section 2.3 (see example in Fig. 7).

As an example, Fig. 10a shows the global stress and normalized displacement for one representative experiment, the Tensylon 30A off-axis angle 15° high-rate (TEN-15DEG-C01) specimen. For the off-axis loading specimens, load generally increases linearly, softening as maximum stress is approached, and then fails in shear (sliding). Yield stress refers to the global engineering stress at which the load is no longer increasing linearly; for Fig. 10, it corresponds to time = 66 μs. Figure 11 shows a series of DIC maximum shear strain profiles from this experiment for select normalized displacement levels, corresponding to the numbered blue marks in Fig. 10a. In the images, the incident bar is at the left; the number refers to the time in microseconds, with the first image occurring at t = 40 μs and the final image occurring at t = 90 μs. For this specimen, strain concentrates at two locations, which are marked as A and B in the final strain profile (at 90 μs). Shear failure at location A occurred slightly earlier than at location B.

After peak stress (66 μs), the specimen starts to buckle due to shear instability, and changes shape (becoming more rhombic). This specimen shape change, from rectangular to rhombus, can be seen in Fig. 11 (note change in shape relative to reference red bars). Figure 10b shows the averaged maximum shear strain at locations A and B, as well as global stress, as a function of time. For this specimen, the shear strain rate is obtained by calculating a linear fit of the average maximum shear strain over the range of 20–80 MPa global engineering stress (~36–64 μs) and then averaging these two fits. For most of the experiments, failure concentrated at a single location, so no averaging was required. The appendix contains the remaining strain profiles to complete the set of 15° experiments (low rate, intermediate rate, and high rate for both Tensylon 30A and HB25), as well as the strain profiles for the complete set of 30° experiments.

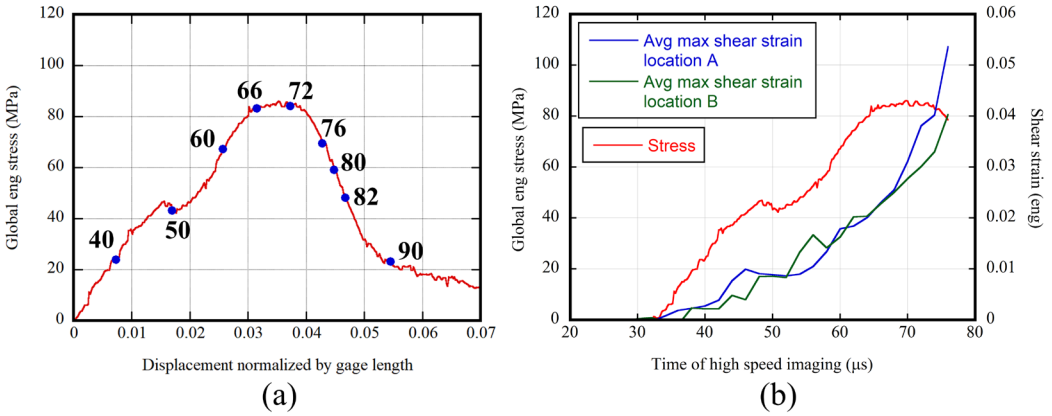

Fig. 10 Tensylon 30A off-axis 15° high-rate specimen (TEN-15DEG-C01). (a) Global stress as a function of normalized displacement with blue dots locating corresponding strain profiles in Fig. 11. Dot numbers are time in microseconds for corresponding high-speed imaging. (b) Global stress (left axis) and shear strain (right axis) plotted as a function of time of high-speed imaging. The average maximum shear strain is plotted at the failure locations A and B, which are identified in Fig. 11.

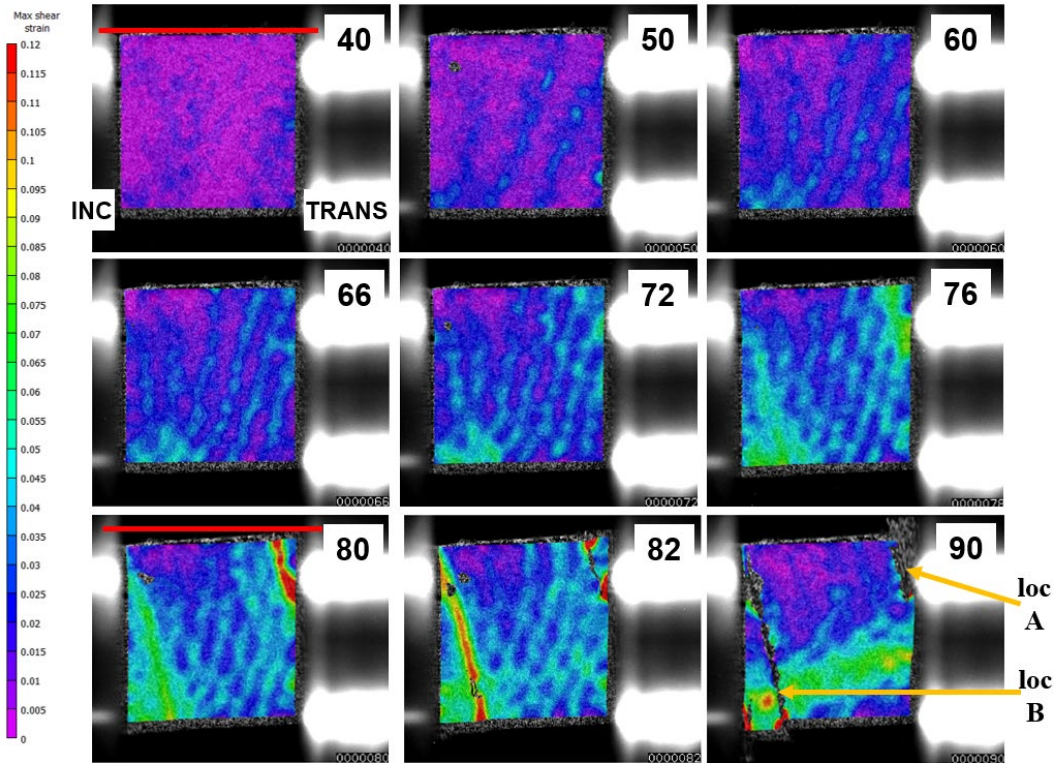

Fig. 11 Tensylon 30A off-axis 15° high-rate specimen (TEN-15DEG-C01) maximum shear strain profiles. The number in the upper-right corner of each profile indicates the image capture time (in microseconds) and corresponds to the blue marks in Fig. 10a and the x-axis in Fig. 10b. For all profiles of Fig. 11, the incident bar was on the left and the transmission bar was on the right, which are labeled in the 40-µs profile as "inc" and "trans," respectively. In the 40-µs profile, the top of the specimen is traced with a horizontal red bar. A similar horizontal red bar is included in the 80-µs profile to demonstrate how the specimen changed shape into a rhombus during loading.

3.1 Tensylon 30A

3.1.1 Effect of Off-Axis Angle at Constant Loading Rate

Characterizing the high-rate response of off-axis angle shear loading of UHMWPE composites was the priority for this study; hence a larger range of off-axis angles was used at this loading rate for Tensylon 30A. A large drop-off in strength and elastic stiffness was observed as the off-axis angle orientation changed from normal to larger angles. This reduction appeared to reach a minimum at the 30° orientation; for the other loading rates and material, off-axis shear experiments were focused on the 0°–30° range. The global response of Tensylon 30A off-axis loading at different off-axis angles is shown in Figs. 12–14 for high, low, and intermediate rates, respectively. A significant effect of off-axis loading angle on the global response was observed, with increasing angle leading to softer response.

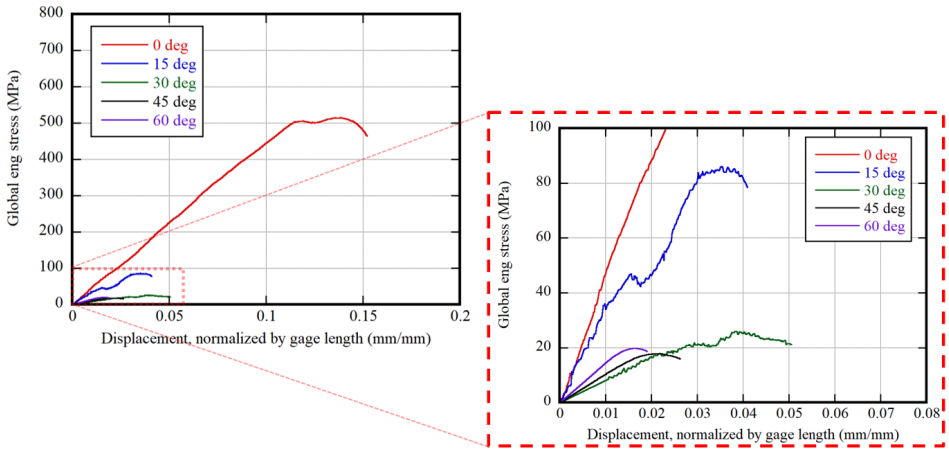

Fig. 12 Global response of Tensylon 30A off-axis loading at high rate as a function of angle

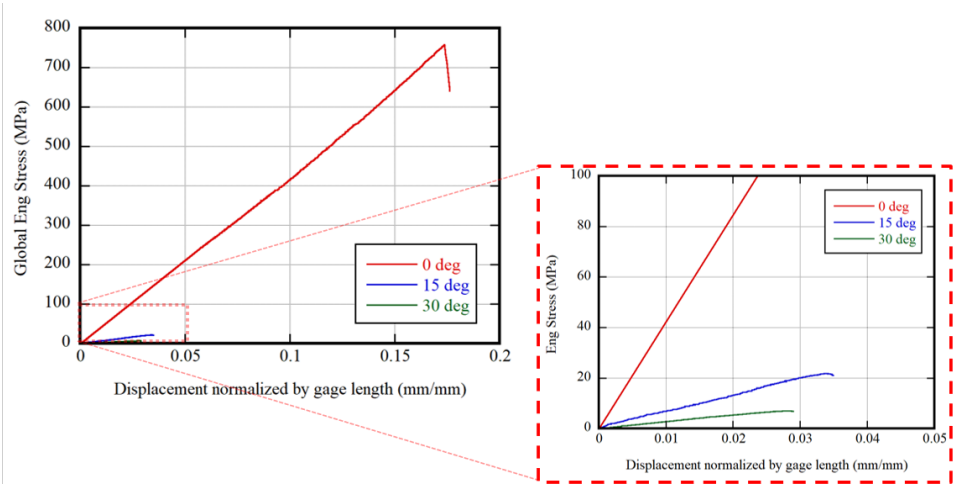

Fig. 13 Global response of Tensylon 30A off-axis loading at low rate as a function of angle

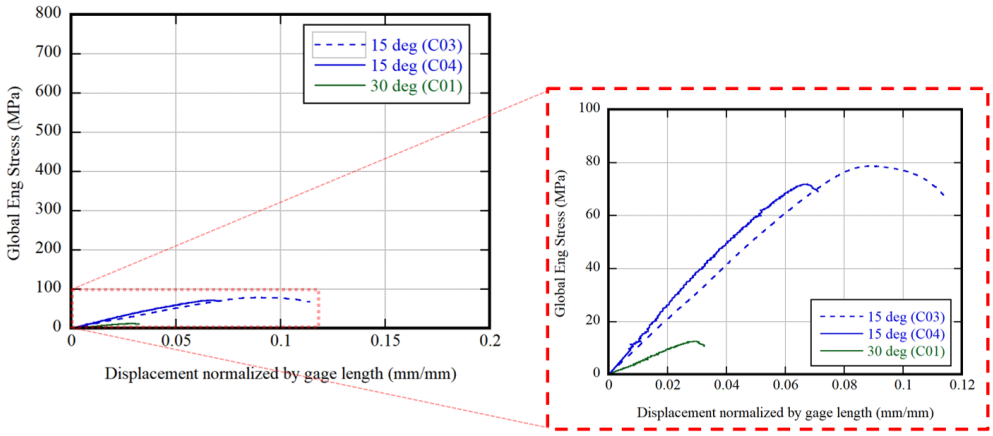

Fig. 14 Global response of Tensylon 30A off-axis loading at intermediate rate as a function of angle. Note: no normal orientation (0°) experiment was performed.

3.1.2 Effect of Loading Rate at Constant Off-Axis Angle

Figure 15 shows the global engineering stress versus normalized displacement for Tensylon 30A at UD layer orientation normal to loading axis (0° angle). At this normal orientation, there was no obvious strain rate effect on specimen global stiffness, with all three experiments having similar stiffness. The failure strength of the one high-rate specimen that failed (labeled as C01) was lower than the failure strength of the low-rate specimen. There is no other research suggesting that composite strength decreases with increasing loading rate, and therefore no conclusion of that can be drawn from two specimens.

At 15° off-axis angle orientation, there was a loading rate effect on specimen global stiffness and failure stress, with increasing loading rate resulting in higher stiffness and strength, as shown in Fig. 16. Specimen C03 had slower unloading after failure as the remaining specimen pieces continued to carry load.

At 30° off-axis angle orientation, there was a loading rate effect on specimen global stiffness and failure stress, with higher loading rate leading to higher stiffness and stress. Figure 17 shows the global engineering stress versus normalized displacement response for Tensylon 30A at 30° off-axis orientation.

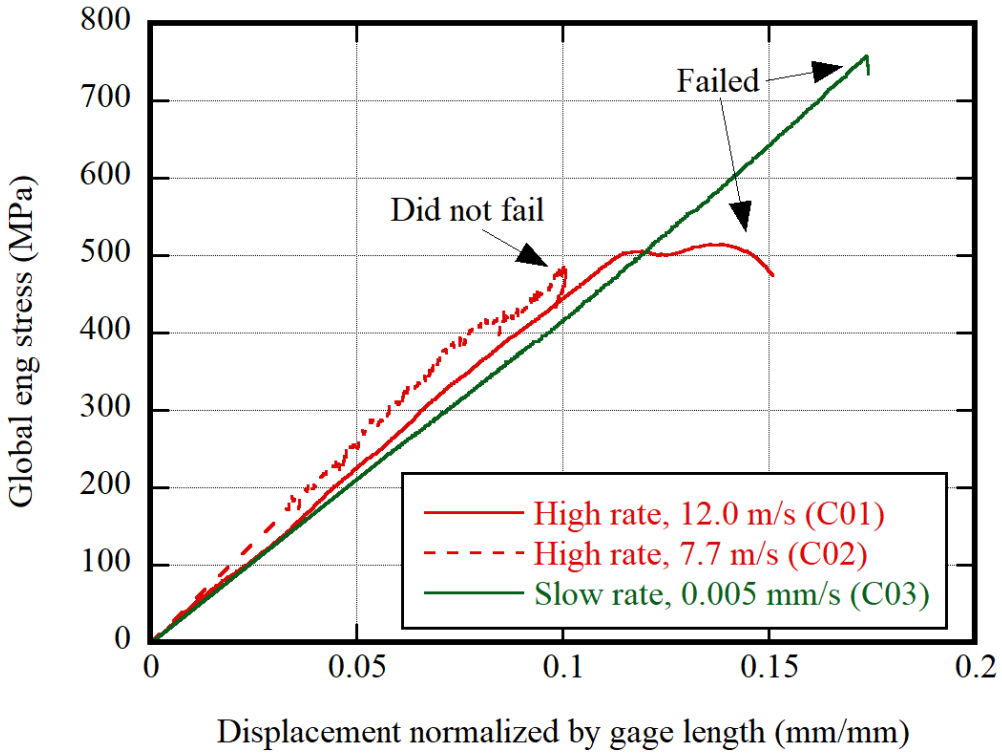

Fig. 15 Global response of Tensylon 30A for normal orientation (0°) off-axis shear specimens as a function of loading rate. Note: no intermediate rate experiment was performed.

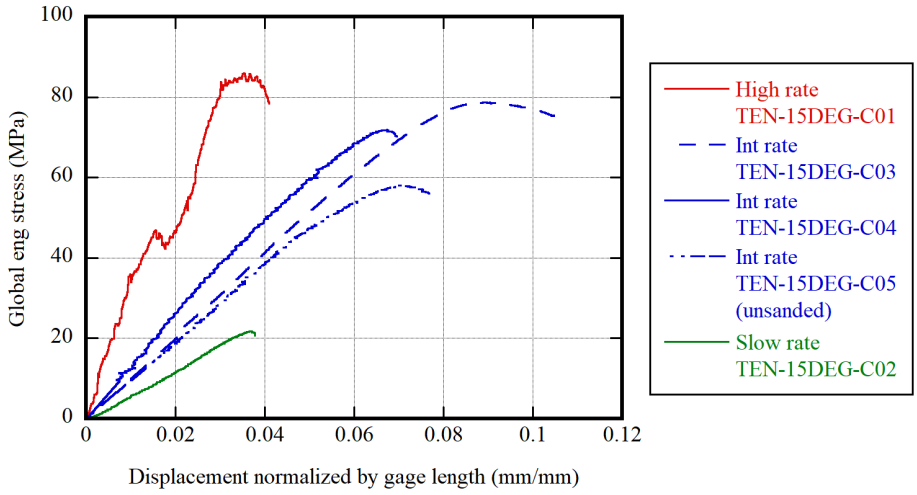

Fig. 16 Global response of Tensylon 30A 15° off-axis shear specimens as a function of loading rate

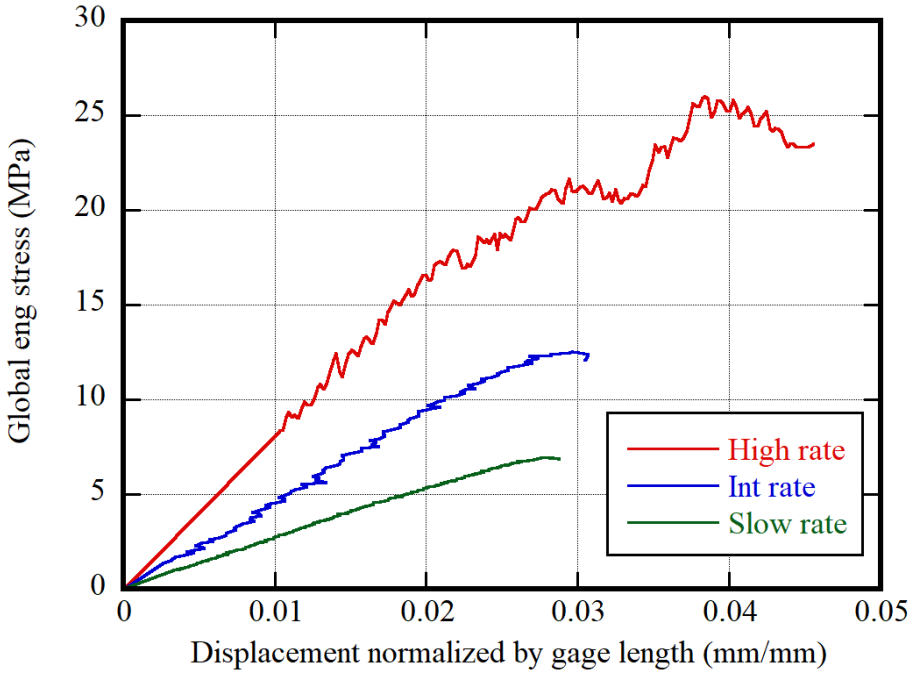

Fig. 17 Global response of Tensylon 30A 30° off-axis shear specimens as a function of loading rate

3.2 Dyneema HB25

3.2.1 Effect of Off-Axis Angle at Constant Loading Rate

Three off-axis shear loading angles were studied for Dyneema HB25 loaded at high rate: 0°, 15°, and 30°. A large drop-off in yield stress was observed as the off-axis angle orientation changed from normal to 30° angle. Stiffness was also reduced as the angle changed from 0° to 15°; stiffness was approximately constant as the angle changed from 15° to 30°. Figure 18 shows the global response of Dyneema HB25 off-axis loading at high rate as a function of off-axis angle. The normal orientation specimen (0°) did not fail at the end of the loading pulse.

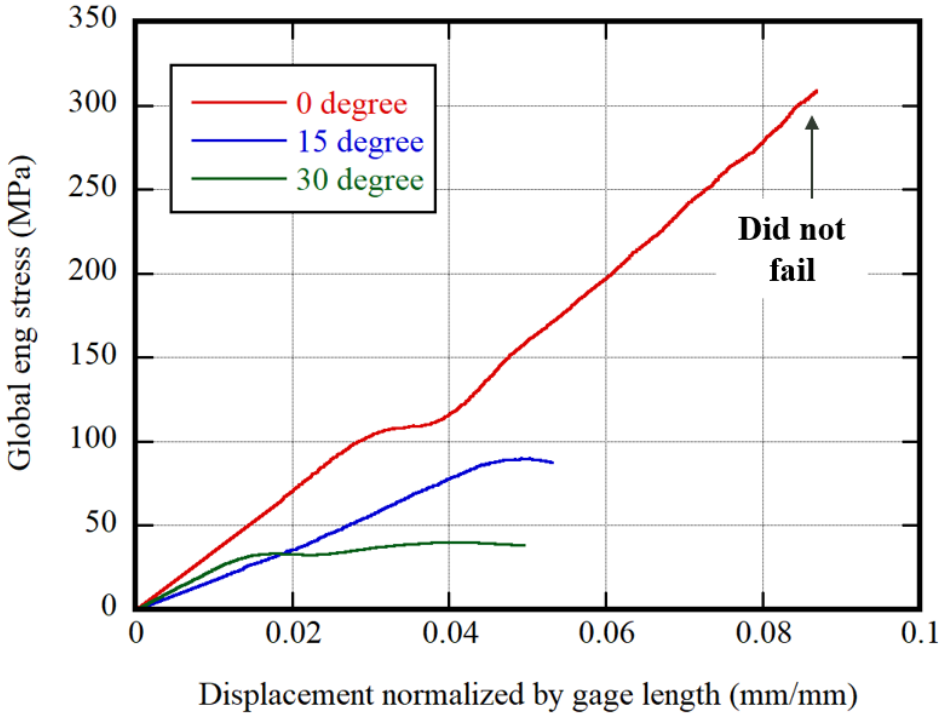

Fig. 18 Global response of Dyneema HB25 off-axis loading at high rate as a function of angle

For the intermediate and low loading rates, off-axis shear loading experiments were performed on 15° and 30° orientations only. For both low and intermediate loading rates, an effect of off-axis angle was apparent, with the smaller angle (15°) having larger modulus and strength compared to the 30° angle at the same loading rate. Figure 19 shows the global response of Dyneema HB25 off-axis loading at (a) intermediate and (b) low loading rate as a function of off-axis angle.

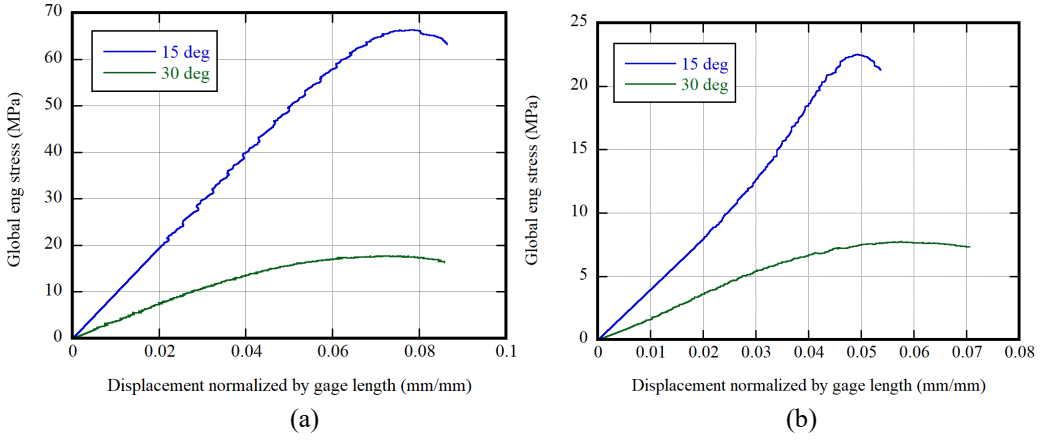

Fig. 19 Global response of Dyneema HB25 off-axis loading at (a) intermediate and (b) low rate as a function of angle

3.2.2 Effect of Loading Rate at Constant Off-Axis Angle

At the 15° angle orientation for Dyneema HB25, there was a strain rate effect, with increasing loading rate corresponding to larger modulus and strength. Figure 20 shows the global engineering stress versus normalized displacement for HB25 at 15° orientation. This trend was repeated for the 30° angle, with increasing loading rate corresponding to larger modulus and strength. Figure 21 shows the global engineering stress versus normalized displacement for HB25 at 30° orientation.

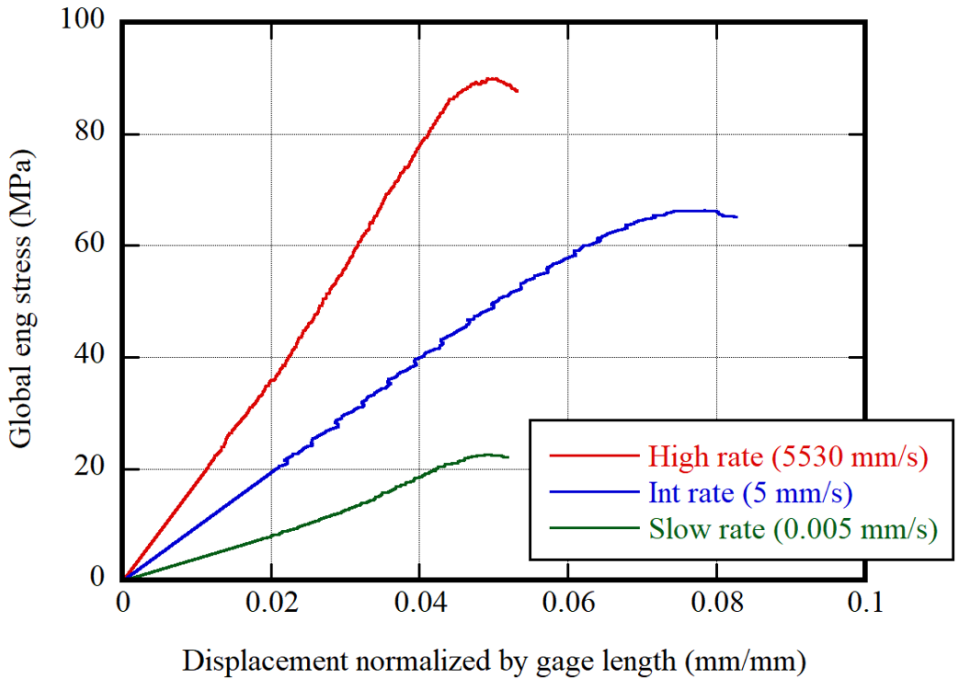

Fig. 20 Global response of Dyneema HB25 15° off-axis shear specimens as a function of loading rate

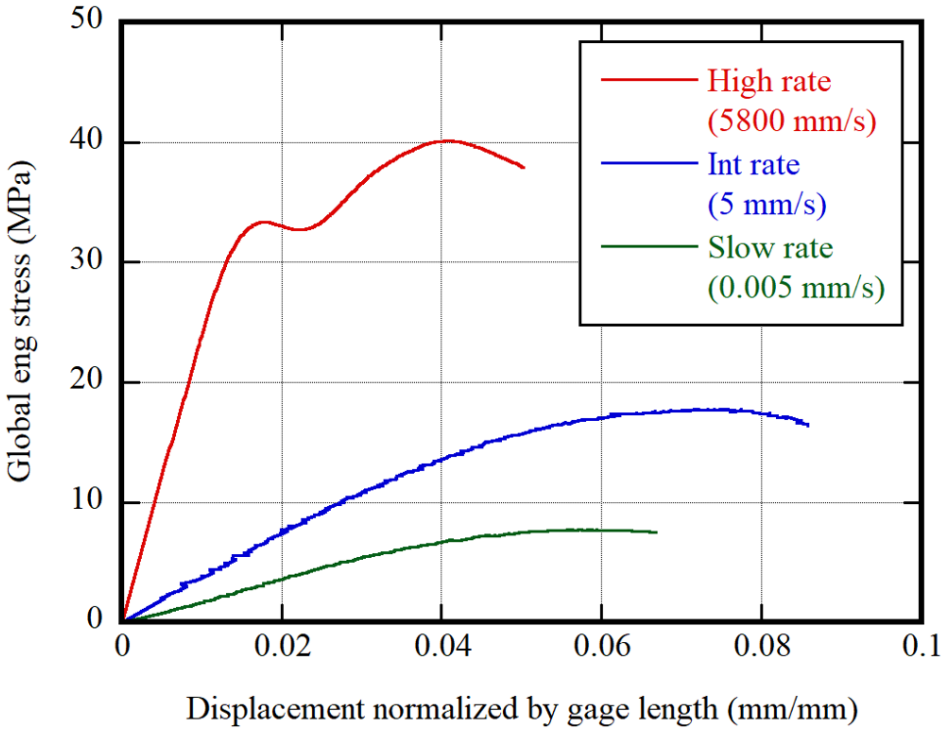

Fig. 21 Global response of Dyneema HB25 30° off-axis shear specimens as a function of loading rate

3.3 Off-Axis Loading Specimen Failure Behavior

Two types of sliding failure were observed during these experiments. Some specimens had full ply sliding failure, where failure occurred at a ply location that spanned the entire specimen. Others had partial ply failure localized near one of the corners. Examples of the full ply failure are shown in Fig. 22. Examples of the partial ply failure are shown in Fig. 23. There was no distinguishable pattern of failure types with loading rate or off-axis angle. In fact, both failure types could occur in a single specimen (Fig. 24). It is likely that the difference in failure behavior is driven by the presence of defects located randomly throughout the panels or created during the specimen fabrication process.

As an additional example, Fig. 24 shows the Dyneema HB25 off-axis 30° high-rate specimen global stress as a function of normalized displacement and corresponding strain profiles; the global stress contains blue dots that correspond to the strain profiles. This specimen had failure in both modes; partial ply failure occurred first (marked as initial failure in Fig. 24F). After that, the remaining specimen was reloaded, and a subsequent full ply failure occurred (later failure in Fig. 24H).

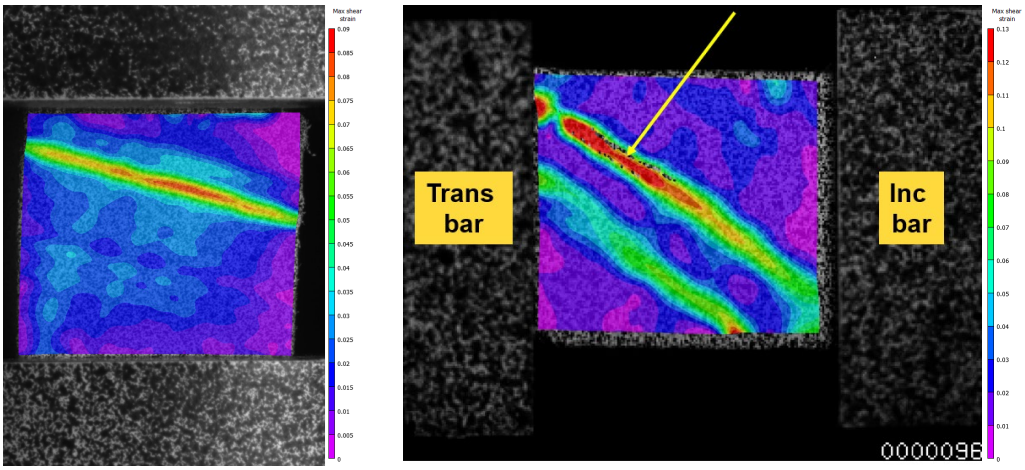

(a) (b)

Fig. 22 Examples of full ply failure for specimens (a) Tensylon 15° at low rate (TEN-15DEG-C02) and (b) Tensylon 60° at high rate (TEN-60DEG-C02)

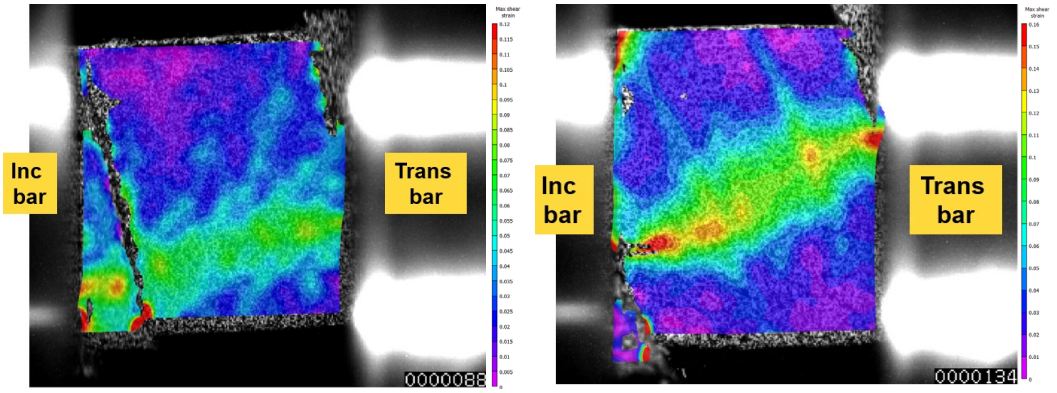

(a) (b)

Fig. 23 Examples of partial ply failure for specimens (a) Tensylon 15° at high rate (TEN-15DEG-C01) and (b) Tensylon 30° at high rate (TEN-30DEG-C01)

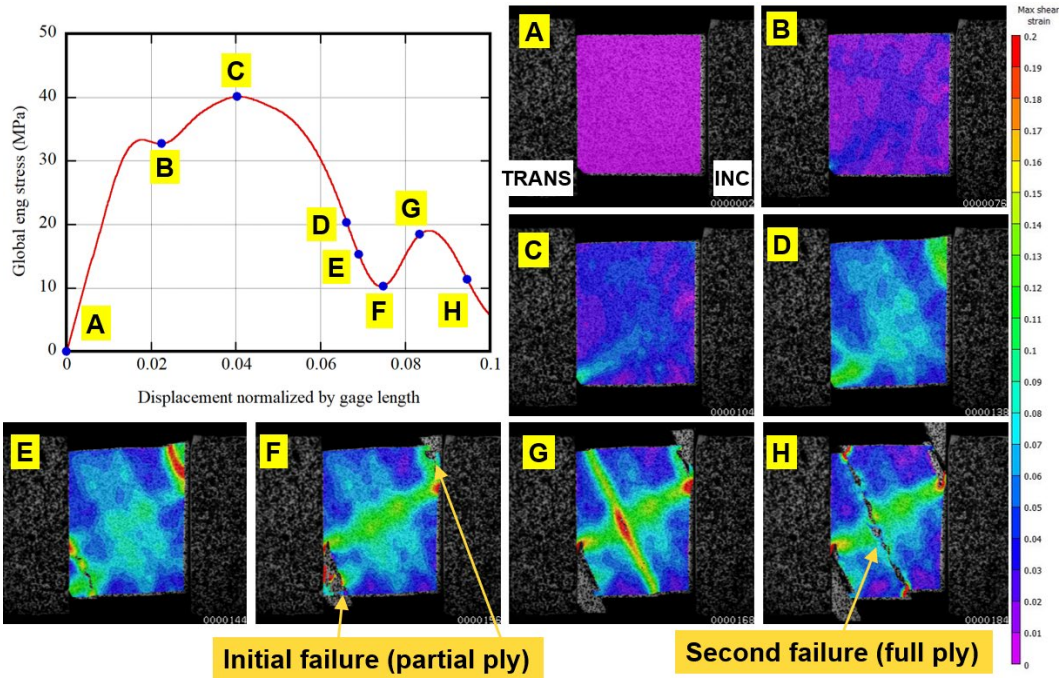

Fig. 24 Dyneema HB25 off-axis 30° high-rate specimen global stress as a function of normalized displacement with marks locating corresponding strain profiles

4. Discussion and Limitations

4.1 Dynamic Equilibrium at High Rate

Dynamic stress equilibrium for high-rate experiments is important to verify to ensure that the stress state within the specimen is known to be constant during loading. This was verified for the high-rate experiments documented here by comparing the specimen interface loads for both the incident bar–specimen interface (I_1) and specimen–transmission bar interface (I_2). For the high-rate experiments here, it was verified that stress equilibrium was achieved with the wave shaping employed. Figure 25 shows the typical load histories for I_1 and I_2 for the Dyneema HB25 off-axis 15° high-rate specimen.

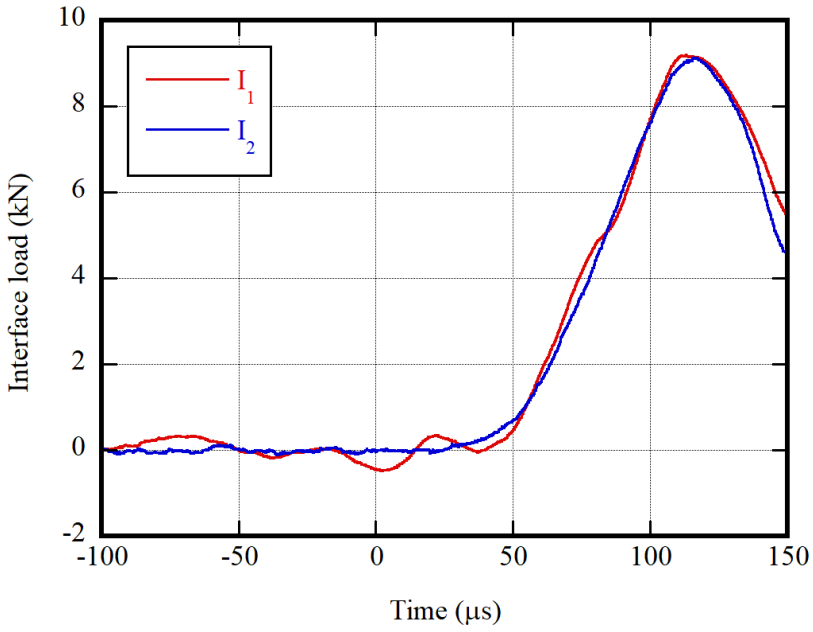

Fig. 25 Interface load vs time for Dyneema HB25 off-axis 15° high-rate specimen (HB25-15DEG-C01) at both bar–specimen interfaces

4.2 Spatial Averaging with DIC

Optical measurements of strain in specimens that contain strain gradients are sensitive to DIC analysis parameters, such as subset size and step size (Jones and Iadicola 2018). Subset size dictates the area over which DIC performs spatial averaging; larger subset sizes produce strain data averaged over a larger area. This has the effect of decreasing the magnitude of strain in areas that have strain gradients if the subset size is not small enough (Gunnarsson et al. 2021). For the experiments documented here, the strain concentrations are small and strain gradients large, so the strain data is dependent on the analysis parameters.

4.3 Comparison of Sanded and Non-sanded Specimens

Preparing the specimens to have flat and parallel loading surfaces by sanding was a time-intensive process. To evaluate the time-intensive sanding of specimens, one specimen was off-axis shear loaded without any sanding at all, Tensylon at intermediate rate and 15° orientation (C05). Figure 26 shows the global engineering stress response for all three Tensylon 15° orientation specimens at intermediate rate (C03, C04, C05). The un-sanded specimen had the lowest modulus and strength of all three specimens, although it is difficult to draw conclusions about the effect of sanding from a single experiment. This suggests that the small amount of specimen heating that may occur during sanding does not cause a softening in the mechanical response.

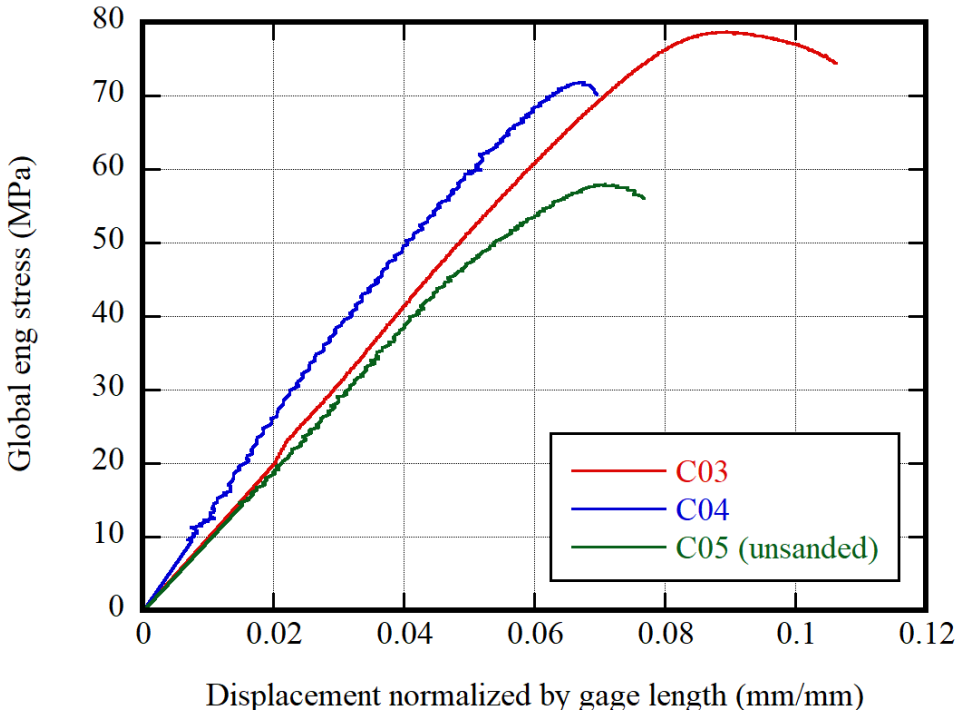

Fig. 26 Global response of Tensylon 30A 15° off-axis shear specimens at intermediate rate

5. Conclusions

The ILSR of UHMWPE composites was characterized by loading specimens at off-axis angles relative to the plane of the UD layers. The method was applied to two different classes of UHMWPE laminates: film-based and fiber-based. The experiments were specifically designed to provide interlaminar shear failure that has been lacking for these materials.

The strain rate effect on the ILSR was characterized for these materials for the first time by applying off-axis loading at low, intermediate, and high rate. At 15° and 30° off-axis angles, the stiffness and strength increased with strain rate in both materials. Normalized failure displacement did not monotonically increase with strain rate; specimens loaded at intermediate rate failed at larger normalized displacements than either low or high rate. This method allowed the full-field deformation of the specimen surface to be imaged during loading and failure. Shear strain was then calculated at the locations of failure using DIC analysis. Comparing specimen shapes during deformation elucidated operative failure mechanisms. The UHMWPE composites experienced a brittle type of failure at high rate, where specimens catastrophically failed after a small shape deformation, becoming rhombic. This shape deformation was more pronounced at the low and intermediate rates.

The utility of these experiments to the research community has been demonstrated. The loading responses and the deformation images have provided the physical basis for recent computational models simulating the rate-dependent loading response of UHMWPE incorporating the observed shear Mode-2 delamination failure. Specifically, Alexander et al. (2023) have used the 15° Tensylon experiments reported here to optimize their computational framework, which models UHMWPE at the subscale level of individual UD layers and incorporates interlayer delamination.

6. References

Alexander SL, Becker R, Weerasooriya T. An experimental-computational framework for UHMWPE films based on deformation and failure mechanisms: general approach and application to off-axis shear loading. DEVCOM Army Research Laboratory (US); 2023 Oct. Report No.: ARL-TR-9811.

Alexander SL, Weerasooriya T. Mechanical characterization of advanced ultra-high molecular weight polyethylene (UHMWPE) composites by ultrasonic method. DEVCOM Army Research Laboratory (US); 2021 Aug. Report No.: ARL-TR-9254.

Bogetti TA, Walter M, Staniszewski J, Cline J. Interlaminar shear characterization of ultra-high molecular weight polyethylene (UHMWPE) composite laminates. Composites Part A: Applied Science and Manufacturing. 2017 Jul 1;98:105–15.

Chen WW, Song B. Split Hopkinson (Kolsky) bar: design, testing and applications. Springer Science & Business Media; 2010 Nov 11.

Cline J, Love B. The effect of in-plane shear properties on the ballistic performance of polyethylene composites. Int J Impact Eng. 2020;143:103592.

Fourest T, Berthe J. Experimental investigation of the strain-rate effects on the failure of composite materials with off-axis tensile tests on unidirectional plies. Strain. 2021 Aug;57(4):e12385.

Gunnarsson CA, Alexander SL, Weerasooriya T. Bending response of human skull-beams as a function of loading rate and loading tip-geometry. US Army Combat Capabilities Development Command, Army Research Laboratory; 2021 July 1. Report No.: ARL-TR-9215. https://apps.dtic.mil/sti/pdfs/AD1142091.pdf

Hosur MV, Alexander J, Vaidya UK, Jeelani S, Mayer A. Studies on the off-axis high strain rate compression loading of satin weave carbon/epoxy composites. Composite Structures. 2004 Jan 1;63(1):75–85.

Jones EM, Iadicola MA. A good practice guide for digital image correlation. International Digital Image Correlation Society. 2018;10.

Liu BG, Kandan K, Wadley HN, Deshpande VS. High strain rate compressive response of ultra-high molecular weight polyethylene fibre composites. International Journal of Plasticity. 2019 Nov 1;122:115–34.

Meshi I, Amarilio I, Benes D, Haj-Ali R. Delamination behavior of UHMWPE soft layered composites. Composites Part B: Engineering. 2016 Aug 1;98:166–75.

Ninan L, Tsai J, Sun CT. Use of split Hopkinson pressure bar for testing off-axis composites. International Journal of Impact Engineering. 2001 Mar 1;25(3):291–313.

Reddy PR, Reddy TS, Srikanth I, Kushwaha J, Madhu V. Development of cost effective personnel armour through structural hybridization. Defence Tech. 2020 Dec 1;16(6):1089–97.

Schreier H, Orteu JJ, Sutton MA. Image correlation for shape, motion and deformation measurements: basic concepts, theory and applications. Springer-Verlag US; 2009.

Singletary J, Lauke B. Polyolefin film–reinforced composites for personal protection. Advanced Fibrous Composite Materials for Ballistic Protection. Woodhead Publishing; 2016 Jan 1. p. 389–408.

Appendix. Shear Strain Profiles

Figure 11 presented the maximum shear strain profiles for the Tensylon 30A 15° off-axis specimen loaded at high rate (TEN-15DEG-C01). Section A.1 of this appendix contains the maximum shear strain profiles for the remaining 15° off-axis specimens (Figs. A-1 through A-6) for Tensylon 30A and Dyneema HB25. Thus, the profiles here, together with Fig. 11, provide the complete set of all 15° experiments at all three rates for both Tensylon 30A and Dyneema HB25.

Section A.2 provides the maximum shear strain profiles for the complete set of 30° experiments at all three rates for both Tensylon 30A and Dyneema HB25 (Figs. A-7 through A-12). For each experiment, the strain profile relative to the loading history is indicated by linking the profiles to the loading response via lettered or numbered labels.

A.1 Shear Strain Profiles for 15° Specimens

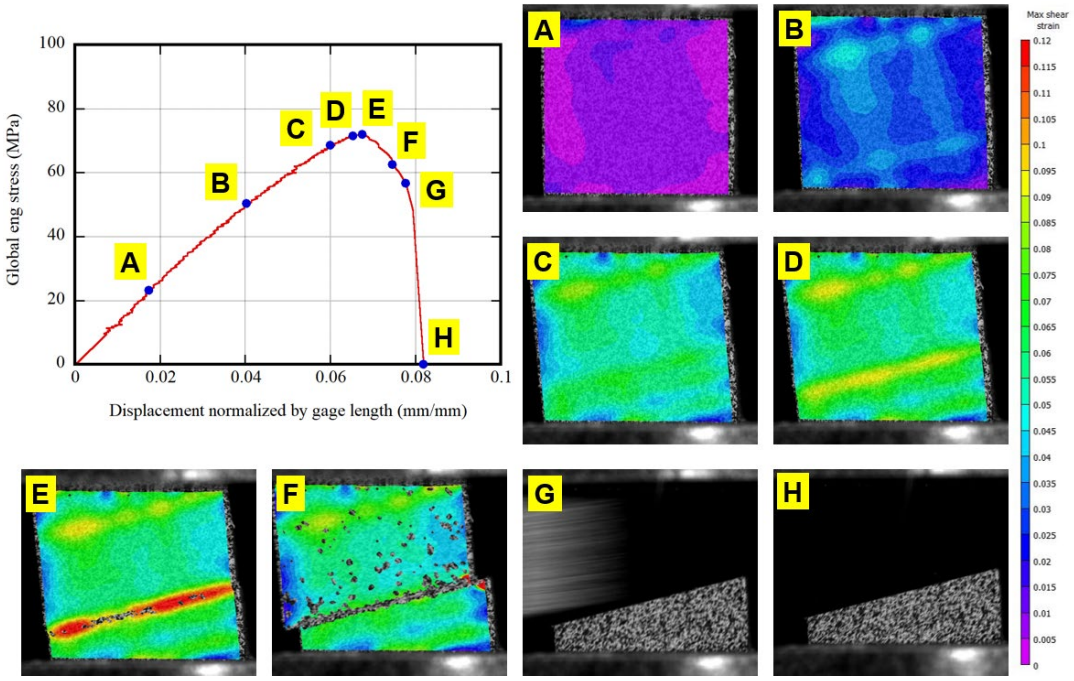

Fig. A-1 Tensylon 30A off-axis 15° intermediate rate specimen (TEN-15DEG-C04) global stress as a function of normalized displacement with marks locating corresponding strain profiles

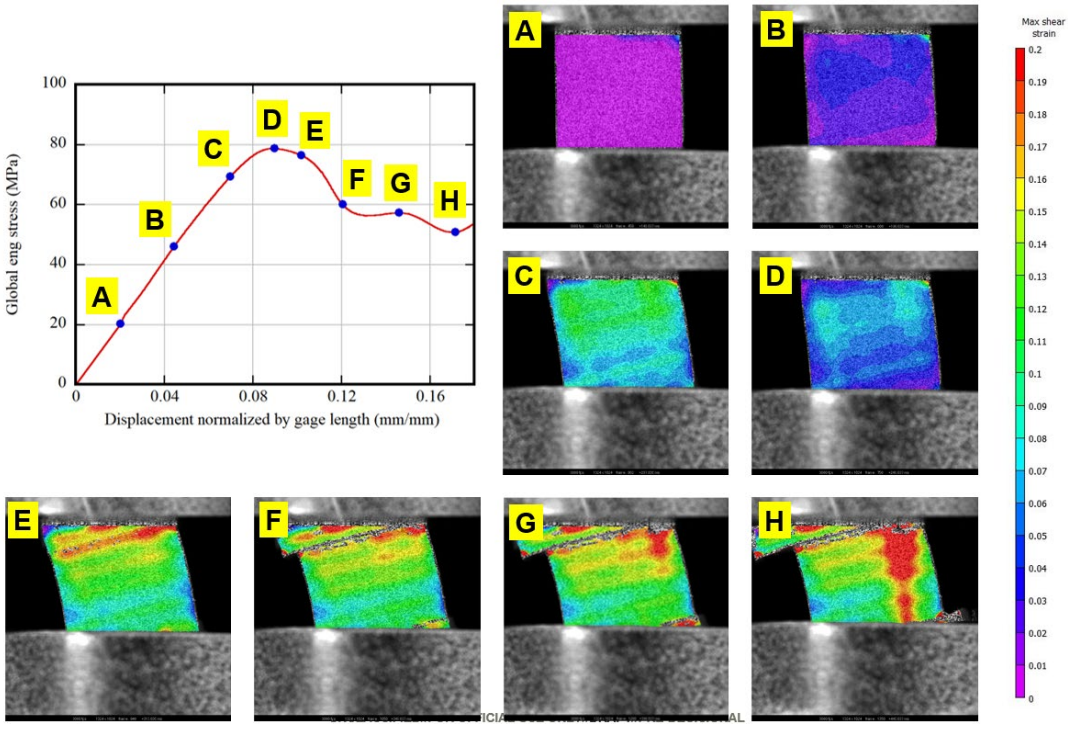

Fig. A-2 Tensylon 30A off-axis 15° intermediate rate specimen (TEN-15DEG-C03) global stress as a function of normalized displacement with marks locating corresponding strain profiles

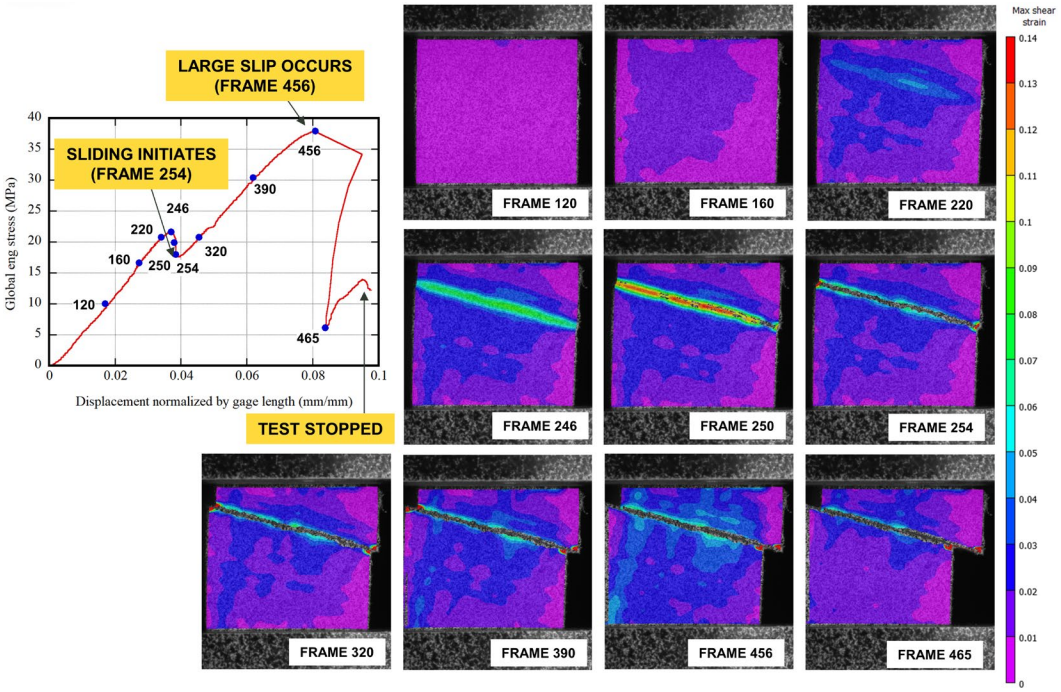

Fig. A-3 Tensylon 30A off-axis 15° low-rate specimen (TEN-15DEG-C02) global stress as a function of normalized displacement with marks locating corresponding strain profiles

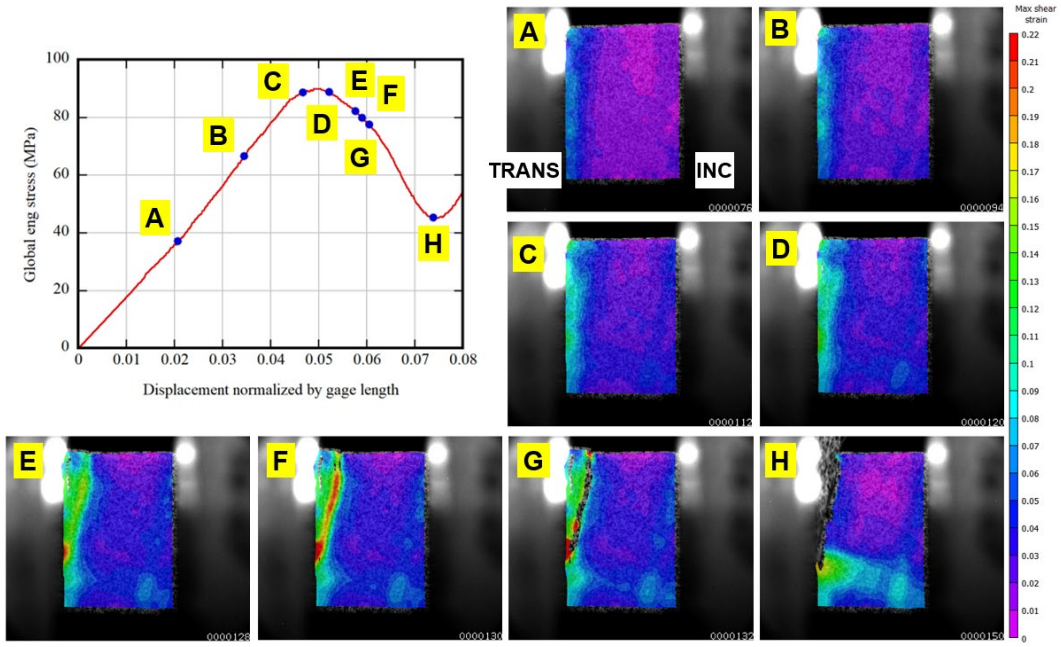

Fig. A-4 Dyneema HB25 off-axis 15° high-rate specimen (HB25-15DEG-C01) global stress as a function of normalized displacement with marks locating corresponding strain profiles

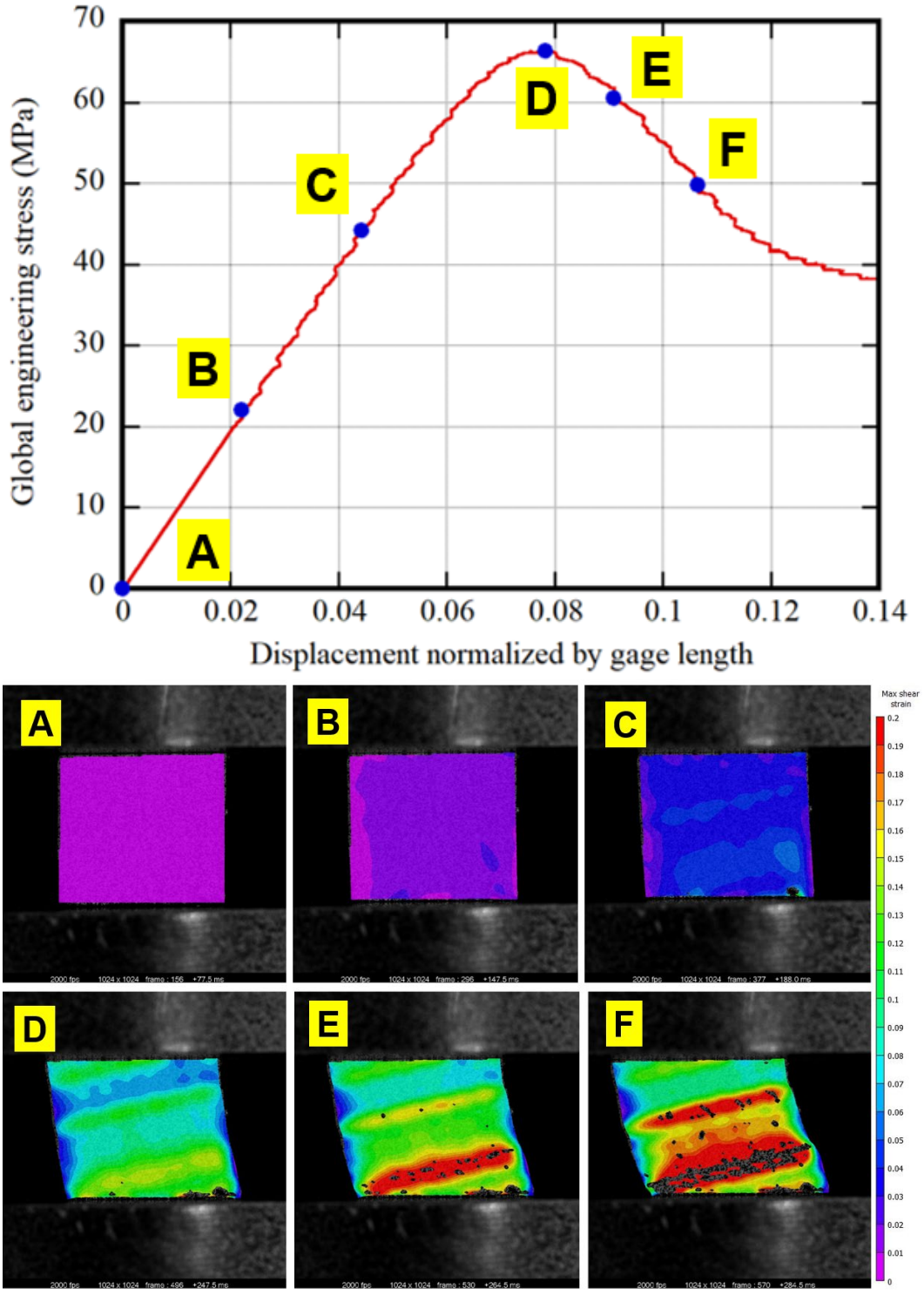

Fig. A-5 Dyneema HB25 off-axis 15° intermediate rate specimen (HB25-15DEG-C04) global stress as a function of normalized displacement with marks locating corresponding strain profiles

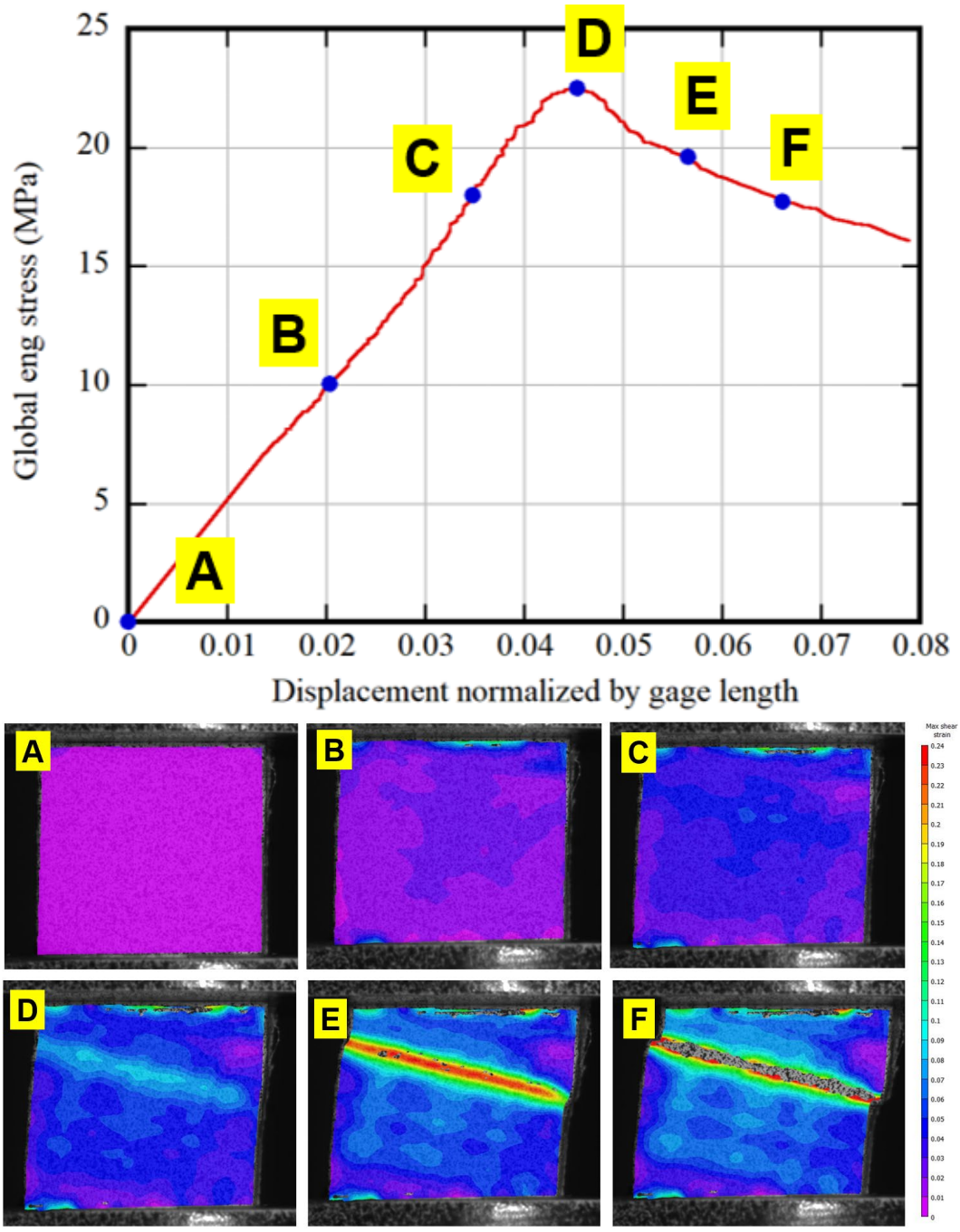

Fig. A-6 Dyneema HB25 off-axis 15° low-rate specimen (HB25-15DEG-C03) global stress as a function of normalized displacement with marks locating corresponding strain profiles

A.2 Shear Strain Profiles for 30° Specimens

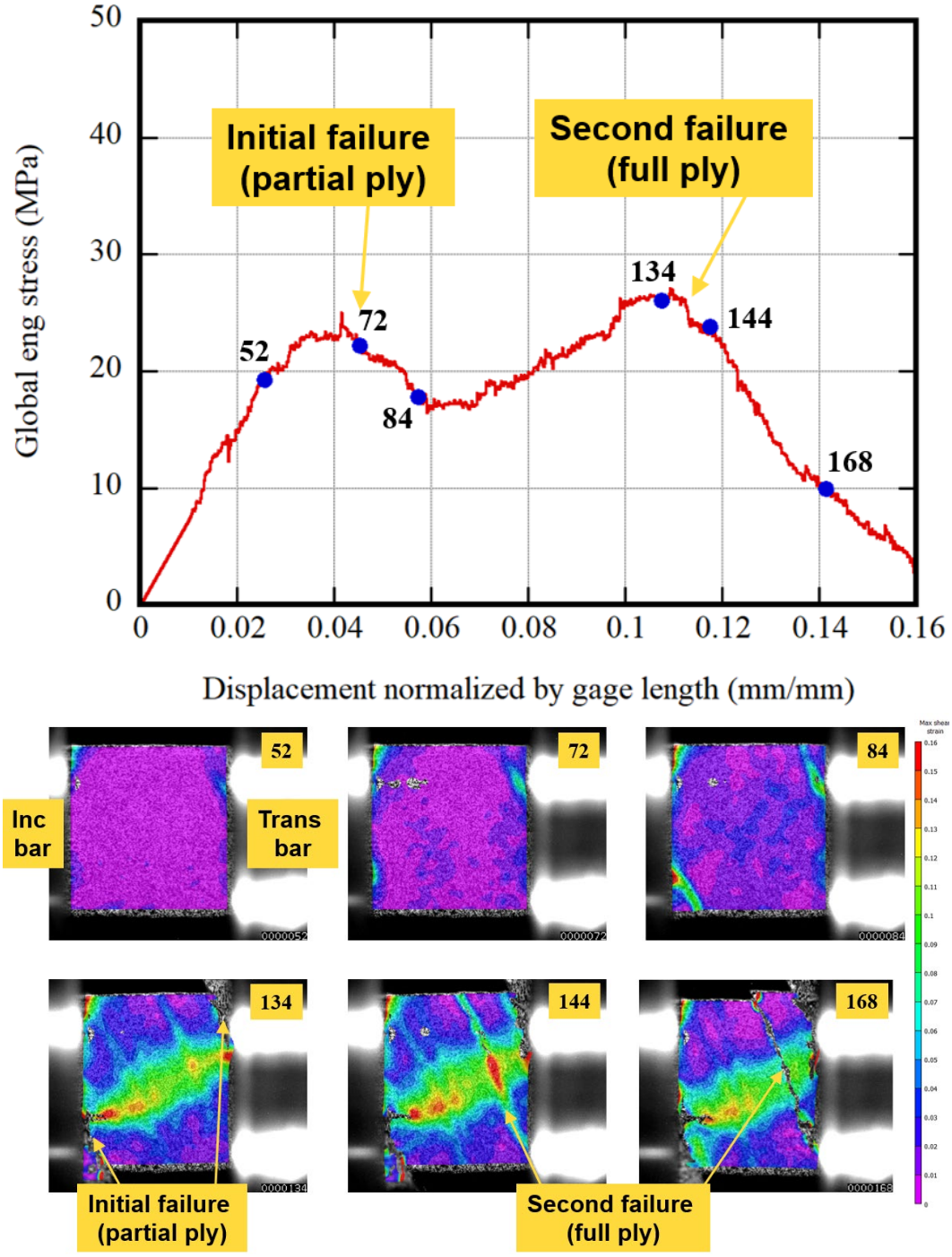

Fig. A-7 Tensylon 30A off-axis 30° high-rate specimen (TEN-30DEG-C01) global stress as a function of normalized displacement with marks locating corresponding strain profiles

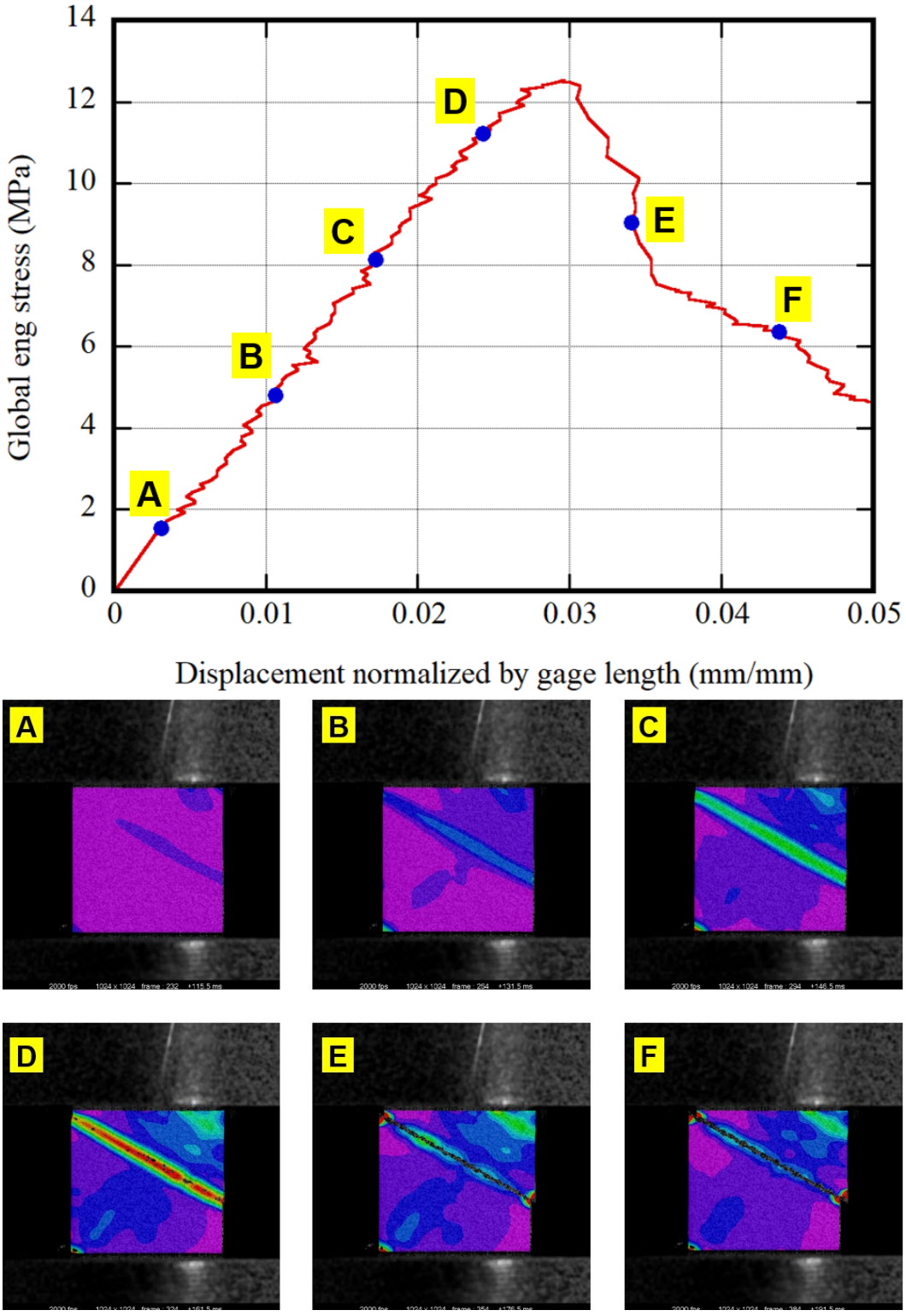

Fig. A-8 Tensylon 30A off-axis 30° intermediate-rate specimen (TEN-30DEG-C03) global stress as a function of normalized displacement with marks locating corresponding strain profiles

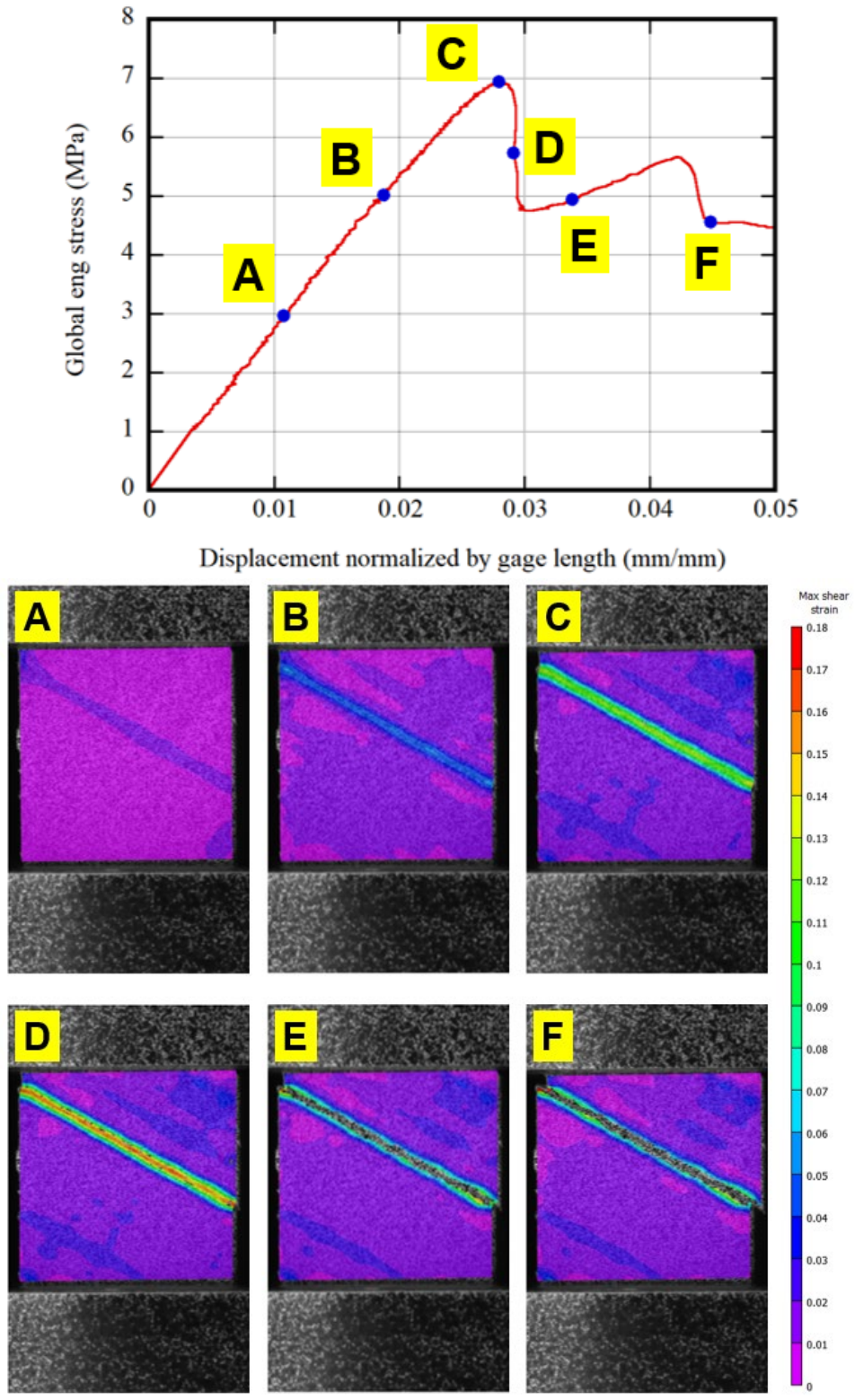

Fig. A-9 Tensylon 30A off-axis 30° low-rate specimen (TEN-30DEG-C02) global stress as a function of normalized displacement with marks locating corresponding strain profiles

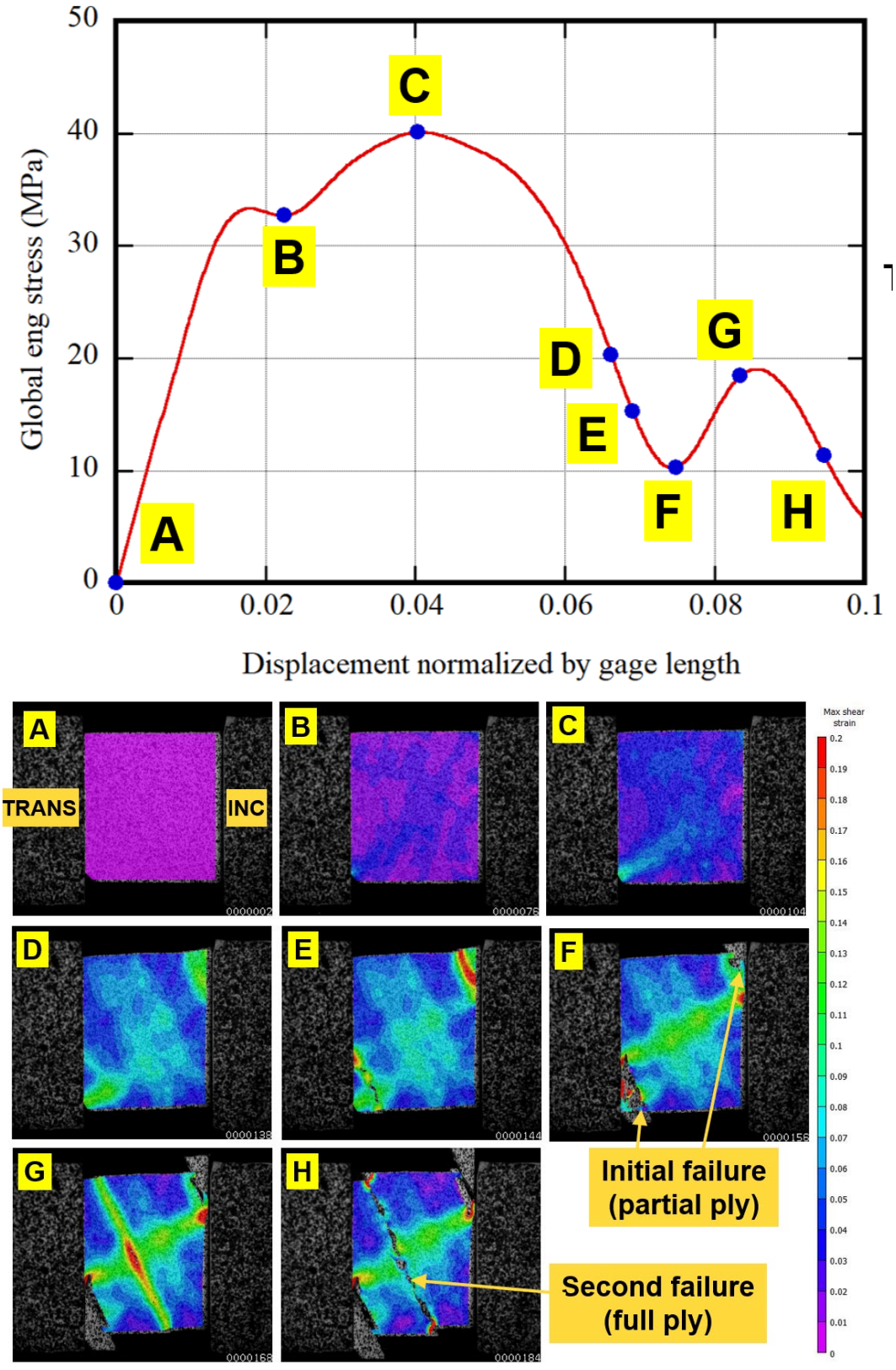

Fig. A-10 Dyneema HB25 off-axis 30° high-rate specimen (HB25-30DEG-C01) global stress as a function of normalized displacement with marks locating corresponding strain profiles

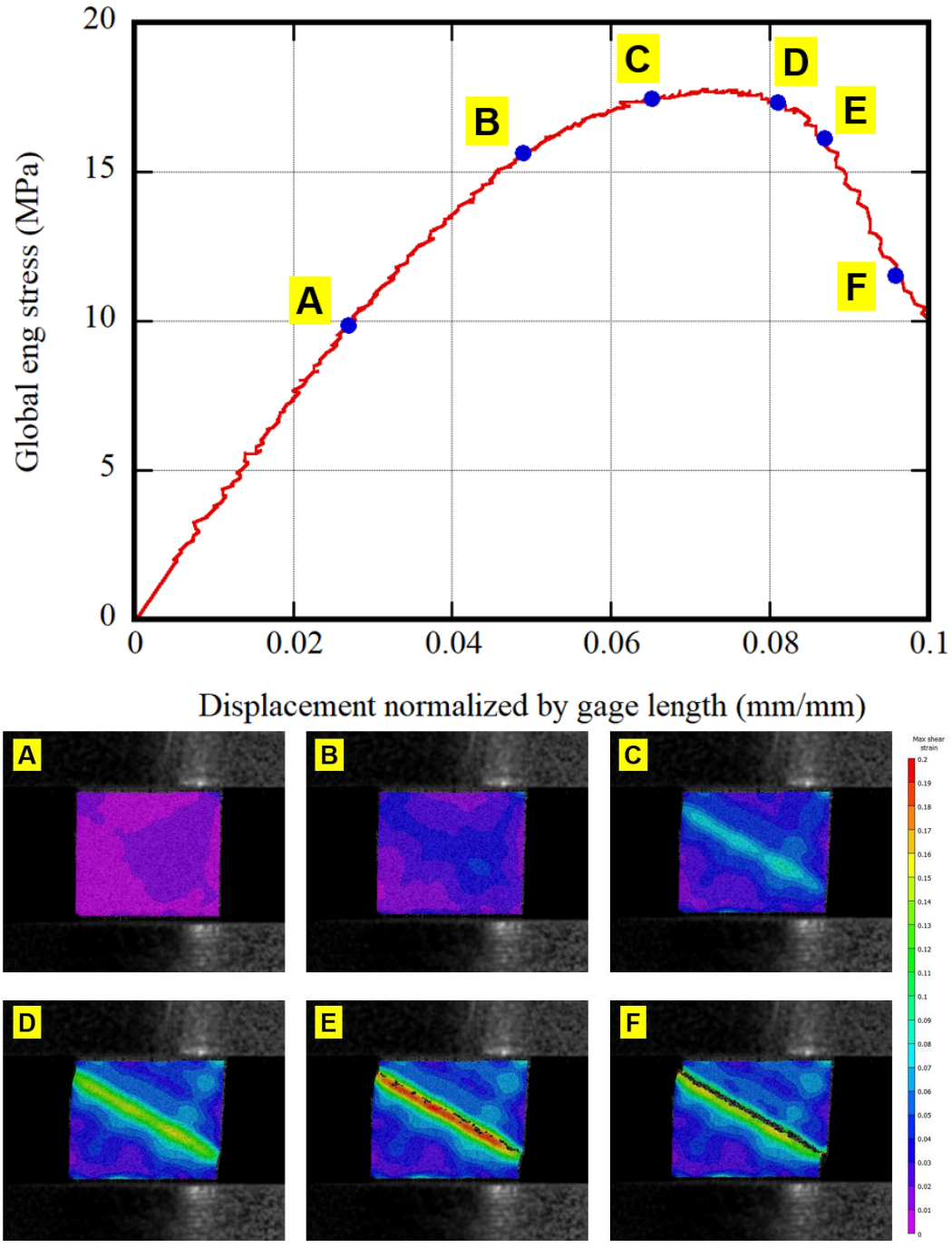

Fig. A-11 Dyneema HB25 off-axis 30° intermediate-rate specimen (HB25-30DEG-C03) global stress as a function of normalized displacement with marks locating corresponding strain profiles

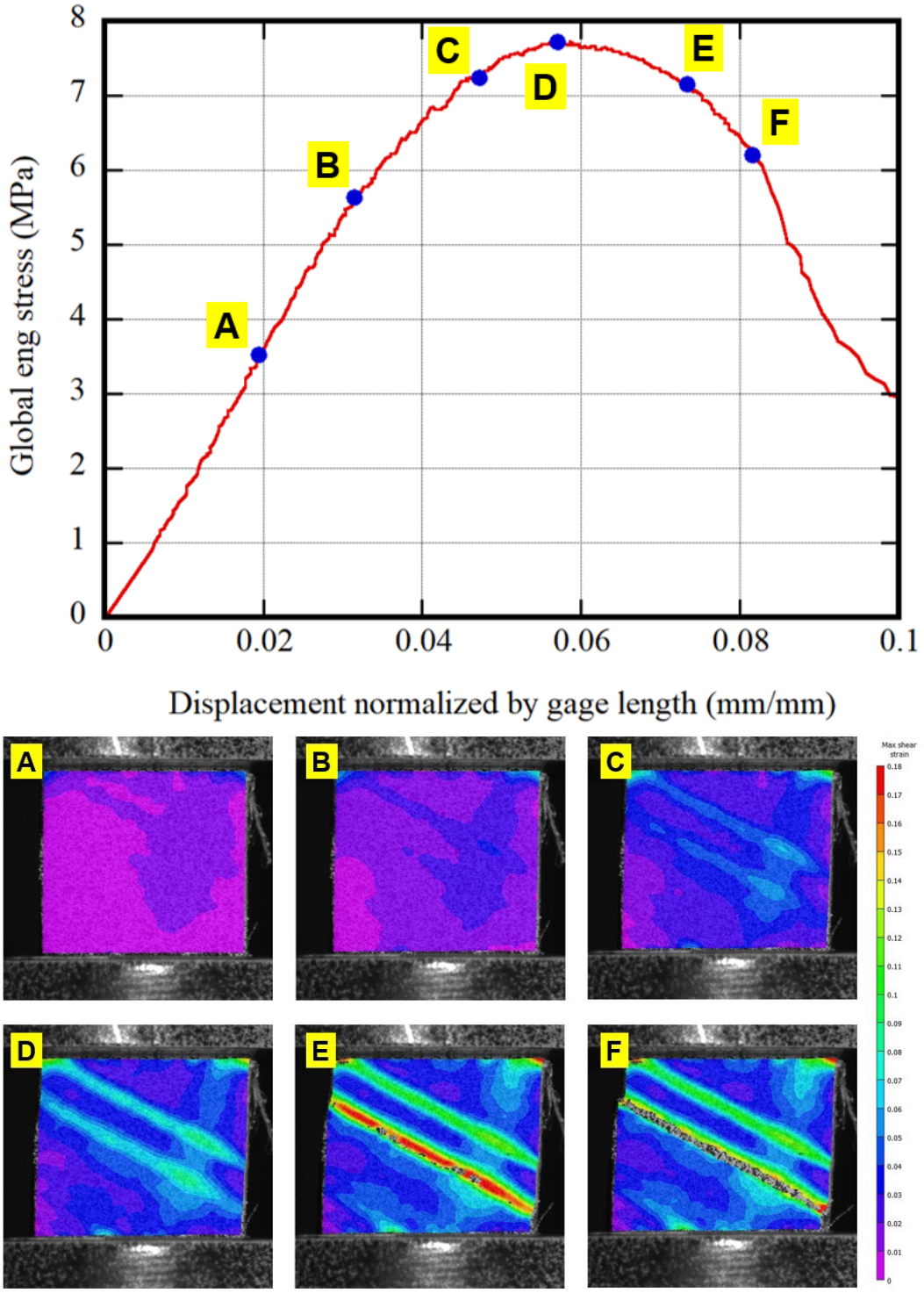

Fig. A-12 Dyneema HB25 off-axis 30° low-rate specimen (HB25-30DEG-C02) global stress as a function of normalized displacement with marks locating corresponding strain profiles

List of Symbols, Abbreviations, and Acronyms

DIC	digital image correlation
fps	frames per second
ILSR	interlaminar shear response
LED	light-emitting diode
max	maximum
SHPB	split Hopkinson pressure bar
SSE	solid-state extrusion
UD	unidirectional
UHMWPE	ultra-high-molecular-weight polyethylene

1 (PDF) DEFENSE TECHNICAL INFORMATION CTR
DTIC OCA

1 (PDF) DEVCOM ARL
FCDD RLB CI
TECH LIB

13 (PDF) DEVCOM SOLDIER CNTR
M G CARBONI
D COLANTO
R DILLALLA
B FASEL
C HEWITT
J KIREJCZYK
R KOLLAR
D KUBIAK
C LINNINGTON
D OTTERSON
J PARKER
W SHAW
A STRZEPEK

4 (PDF) PROG EXECUTIVE OFC SOLDIER
A DEGROOT
J HOPPING
P LOOMIS
N NGUYEN

1 (PDF) PEO IEWS
A FOURNIER

1 (PDF) MTRL SCIENCES DIV
LAWRENCE BERKELY NATL LAB
R RITCHIE

5 (PDF) SOUTHWEST RSRCH INST
C ANDERSON JR
S CHOCRON
D NICOLELLA
T HOLMQUIST
G JOHNSON

2 (PDF) NIST
A FORSTER
M VANLANDINGHAM

1 (PDF) INST FOR DEFNS ANLYS
Y MACHERET

5 (PDF) MRDC DOD BLAST INJURY RSRCH PROGRAM COOR OFC
R GUPTA
A LEWIS
T PIEHLER
R SHOGE
R SPENCER

1 (PDF) USMC
C STEPHENS

4 (PDF) US ARMY AEROMEDICAL RSRCH LAB
F BROZOSKI
V CHANCEY
B MCENTIRE
T ROOKS

1 (PDF) IRREGULAR WARFARE TECH SUPPORT DIR
L TANYAG

1 (PDF) DEVCOM GVSC
R SCHERER

1 (PDF) DEVCOM C5ISR
AMSRD PE
D RUSIN

2 (PDF) DEVCOM CBC
M HORSMON
N VINCELLI

1 (PDF) OSD DOT&E
J IVANCIK

5 (PDF) US NAVAL RSRCH LAB
A BAGCHI
A ILIOPOULOS
J MICHOPOULOS
K TEFERRA
X TAN

4 (PDF) DAC
FCDD DAG S
K LOFTIS
FCDD DAS LBW
G DIETRICH
FCDD DAS LBE
J GURGANUS
S SNEAD

2 (PDF) DEVCOM-ATLANTIC
S COLEMAN
H PIETSCH

3 (PDF) US SOCOM
M CLARK
D GUILLEMIN
N TSANTINIS

144 (PDF) DEVCOM ARL
FCDD RLA A
S KARNA
P FRANASZCZUK
J NEWILL
A RAWLETT
S SCHOENFELD
FCDD RLA B
A WEST
M TSCHOPP
FCDD RLA CB
R BECKER
J CAMPBELL
P GILLICH
C HOPPEL
J LASALVIA
A TONGE
FCDD RLA FF
W HAIRSTON
FCDD RLA HC
A DAGRO
A EIDSMORE
T THOMAS
FCDD RLA M
B CHEESEMAN
K CHO
FCDD RLA MA
K BERNETICH
T BOGETTI
S BOYD
J CAIN
D KNORR
M NEBLETT
E SANDOZ-ROSADO
J SANDS
J STANISZEWSKI
M YEAGER
FCDD RLA MB
G GAZONAS
D GRAY
D MAGAGNOSC
P MOY
D O'BRIEN
J SIETINS
T WALTER
FCDD RLA MC
D CRAWFORD
R JENSEN
J SNYDER
FCDD RLA MD
A BUJANDA
J LA SCALA
E WETZEL
FCDD RLA ME
P PATEL
J SWAB
L VARGAS-GONZALEZ
FCDD RLA MF
K DARLING
D FIELD
A GIRI
S GRENDAHL
C HAINES
K LIMMER
H MURDOCH
FCDD RLA MG
J LENHART
R MROZEK
J ORLICKI
T SIRK
I YEH
FCDD RLA T
M FERMEN-COKER
R FRANCART
T HOLDREN
R YEAGER
FCDD RLA TA
S BILYK
M GRAHAM
S TURNAGE
W UHLIG
C WILLIAMS
FCDD RLA TB
S ALEXANDER
T BAUMER
D CASEM
J CLAYTON
B FAGAN
A GOERTZ
A GUNNARSSON
C HAMPTON
M KLEINBERGER
D KRAYTERMAN
E MATHEIS
J MCDONALD
P MCKEE
C MEREDITH
T PLAISTED
K RAFAELS
S SATAPATHY
L SHANNAHAN
M TEGTMEYER
C WEAVER
T WEERASOORIYA
S WOZNIAK
T ZHANG
FCDD RLA TD

R DONEY
R GUPTA
M KEELE
D KLEPONIS
B KRZEWINSKI
K MASSER
F MURPHY
C RANDOW
S SCHRAML
K STOFFEL
M ZELLNER
FCDD RLA TE
M BURKINS
D GALLARDY
W GOOCH
E KLIER
J LLOYD
M LOVE
P SWOBODA
FCDD RLA TF
J ANGEL
W BRUCHEY
J CAZAMIAS
R COATES
T EHLERS
P JANNOTTI
E KENNEDY
R LEAVY
J LEE
L MAGNESS
D MALLICK
C MEYER
J MONTGOMERY
J RUNYEON
FCDD RLA TG
C CUMMINS
D FOX
N GNIAZDOWSKI
S HUG
S KUKUCK
C PECORA
FCDD RLA V
S SILTON
FCDD RLA VA
R EMERSON
A GHOSHAL
FCDD RLA VB
A HALL
FCDD RLA W
T V SHEPPARD
FCDD RLA WA
J BRENNAN
N TRIVEDI
FCDD RLA WC
M MINNICINO
FCDD RLB
J ZABINSKI
FCDD RLR A
J CIEZAK-JENKINS
D STEPP
FCDD RLR EM
A BROWN
C VARANASI
FCDD RLR ET
B ASHFORD
D COLE
D FORD
FCDD RLR EW
R ANTHENIEN

5 (PDF) WHITING SCHOOL OF ENG
JOHNS HOPKINS UNIV
S BAILOOR
L BRADY
T D NGUYEN
B NOTGHI
KT RAMESH

5 (PDF) GEORGIA INST OF TECH
S KALIDINDI
S MARGULIES
D MCDOWELL
N THADHANI
M ZHOU

1 (PDF) DEPT OF ENGRNG SCI AND MECHANICS
VIRGINIA POLYTECHNIC INST AND STATE UNIV
R BATRA

4 (PDF) MASSACHUSETTS INST OF TECHLGY
INST FOR SOLDIER NANOTECHNOLOGIES
M J BUEHLER
R RADOVITZKY
C SCHUH
S SOCRATE

1 (PDF) DEPT OF MECHL AND NUCLEAR ENGRNG
THE PENNSYLVANIA STATE UNIV
R KRAFT

1 (PDF) INDIAN INST OF TECH
R BHARDWAJ

2 (PDF) CENTER FOR APPLIED BIOMECHANICS
UNIV OF VIRGINIA
M B PANZER
R SALZAR

1 (PDF) UCSD MAT SCI AND ENG
M MEYERS

1 (PDF) WAYNE STATE
BIOMED ENG
CR BASS

3 (PDF) COLLEGE OF ENG
U OF WISC-MADISON
C BRONKHORST
S RUDYKH
R THEVAMARAN

1 (PDF) UNIV OF CAPE TOWN
BLAST IMPACT &
SURVIVABILITY UNIT
T J CLOETE

1 (PDF) UNIV OF OXFORD
BLAST IMPACT
& SURVIVABILITY UNIT
C SIVIOUR

1 (PDF) UNIV OF CAMBRIDGE
ENG DEPT
V DESHPANDE
B LIU

4 (PDF) UNIV OF SOUTH CAROLINA
COL OF ENG
S RAJAN
S SOCKALINGAM
M SUTTON
F THOMAS

3 (PDF) DSM DYNEEMA PROTECTIVE
MATERIALS
U HEISSERER
R ROZANSKY
H VAN DER WERFF

1 (PDF) IMPERIAL COL LONDON
DEPT OF PHYSICS
W PROUD

1 (PDF) DIV OF ENG AND APPL SCI
CALTECH
R RAVICHANDRAN

1 (PDF) DEPT OF AERO ENG AND
ENG MECH
U TEXAS AUSTIN
K RAVI-CHANDAR

1 (PDF) AERO AND ASTRO ENG
PURDUE UNIV
W CHEN

1 (PDF) DEPT OF NEUROSURGERY
MED COL OF WISCONSIN
N YOGANANDAN

1 (PDF) SANDIA NATL LABS
B SANBORN

1 (PDF) WOLFSON SCHOOL OF
MECHANICAL, ELECTRICAL,
AND MANUFACTURING ENG
LOUGHBOROUGH UNIV
V SILBERSCHMIDT

1 (PDF) INSTITUTE SHOCK PHYSICS
WASHINGTON STATE UNIV
V PRAKASH

1 (PDF) MATERIALS SCI AND ENG
UNIV OF DELAWARE
J GILLESPI

1 (PDF) SIBLEY SCHOOL OF MECH
AND AERO ENG
CORNELL UNIV
S L PHOENIX

1 (PDF) DUPONT
B VANARSDALEN

2 (PDF) DEPT OF AERO ENG
UNIV ILLINOIS URBANA-
CHAMPAIGN
J LAMBROS
I CHASIOTIS

1 (PDF) DEPT OF MECH ENG
UNIV CA SANTA BARBARA
S DALY

1 (PDF) UNIV OF MANCHESTER
N BOURNE

1 (PDF) IOWA STATE UNIV
S PATHAK

1 (PDF) CENTER FOR BIOENG AND BIOTECH
UNIV OF WATERLOO
D CRONIN

1 (PDF) DEPT OF MECH ENG
UNIV OF ALBERTA
J HOGAN

1 (PDF) LANGLEY RESEARCH CNTR
NASA
J CLINE

2 (PDF) LOS ALAMOS NATL LAB
E BROWN
G GRAY

1 (PDF) B SCOTT